

Search for H₂O Maser Flares in Regions of Formation of Massive Stars

N. N. Shakhvorostova^{1*}, L. N. Vol'vach², A. E. Vol'vach², A. I. Dmitrotsa²,
O. S. Bayandina¹, I. E. Val'tts¹, A. V. Alakoz¹, N. T. Ashimbaeva³, and G. M. Rudnitskii³

¹*Astro Space Center, Lebedev Physical Institute, Russian Academy of Sciences,
Moscow, 117997 Russia*

²*Crimean Astrophysical Observatory, Russian Academy of Sciences, Nauchnyi,
Republic of Crimea, 298409 Russia*

³*Sternberg Astronomical Institute, Lomonosov Moscow State University,
Moscow, 119992 Russia*

Received February 23, 2018; in final form, April 23, 2018

Abstract—Results of systematic observations of a sample of bright H₂O maser sources with fluxes, on average, exceeding 200 Jy in their main spectral feature during April–September 2017 (G25.65+1.05, G25.825–0.178, G27.184–0.082, G34.403+0.233, G35.20–0.74, G43.8–0.13, G107.30+5.64) are presented. These observations were carried out in preparation for Very Long Baseline Interferometry observations with an array including the Crimean Astrophysical Observatory 22-m radio telescope. All these sources display fairly strong variability during the time interval considered, encompassing fluxes from ~40 to ~2300 Jy. A flare reaching ~17 000 Jy was detected at a velocity of 42.8 km/s in G25.65+1.05 on September 7, 2017, which subsequently grew to 60 000 Jy at the end of September 2017. This suggests the presence of compact maser structures. The velocities covered by various spectral components range from 5 to 20 km/s. In three sources (G25.65+1.05, G25.825–0.178, G35.20–0.74), a general growth in the fluxes of all the spectral features is observed, which may indicate variations in the conditions for pumping by an external source, for example, variations in the infrared flux from a central source or the passage of a shock. Possible evidence for the presence of bipolar outflows or disk structures in G25.65+1.05 is discussed.

DOI: 10.1134/S1063772918090081

1. INTRODUCTION

Numerous peculiar objects accompanying star formation are observed in the interstellar medium. A special place is occupied by sources of molecular maser emission in regions of formation of massive stars, which strongly influence the state of the surrounding matter in the star-forming process. This influence includes heating of the ambient medium, the presence of powerful turbulent motions, and the acceleration of fragmentation of the host molecular cloud, with the subsequent formation of less massive stars. The evolution of the most massive stars is hidden from observations by the high densities and opacities of the matter in the giant molecular clouds in whose cores such stars form, hindering the construction of models for the development of star-forming regions, and especially our understanding of the initial stages in their evolution.

Investigations of mechanisms for the formation of massive stars in molecular clouds and in dense fragments of the interstellar medium located in early

stages of star formation rely on various observational studies of such regions, including systematic observations in various maser lines. Molecular masers arising in the vicinities of massive protostars in various stages of their evolution can provide valuable information about the physical conditions under which they form, since maser pumping is very sensitive to variations of the density and temperature in the corresponding gas–dust condensations embedded in molecular clouds. The most widespread, bright such sources are H₂O masers.

Nearly all H₂O maser lines in star-forming regions display strong variability on time scales from several days to several months (see, e.g., [1, 2]). This variability creates difficulties in source selection and planning for interferometric observations, because it is not possible to predict ahead of time whether the observed flux density will be sufficiently high to be detected on long baselines. On the other hand, the strong variability of H₂O masers indicates that these sources can be treated as indicators of the dynamical environments of star-forming regions. Variations in the radiation field, for example, due to enhancements

*E-mail: nadya@asc.rssi.ru

Table 1. Sources selected for H₂O maser observations on the CrAO 22-m radio telescope

Source	RA J2000	DEC J2000	V _{LSR} , km/s	Distance, kpc	Other names
G25.65+1.05	18 ^h 34 ^m 20.84 ^s	−05°59′42.20″	41.9	2.08 [6]	IRAS 18316−0602, Mol 62, RAFGL 7009S
G25.825−0.178	18 39 03.60	−06 24 11.17	80.3	6.3 [7]	IRAS 18363−0627
G27.184−0.082	18 41 13.21	−05 09 05.13	18.3	1.2 [8]	IRAS 18385−0512
G34.403+0.233	18 53 18.00	+01 25 26.00	54.7	1.5 [9]	IRAS 18507+0121, Mol 74
G35.20−0.74	18 58 13.21	+01 40 35.29	31.2	2.2 [10]	IRAS 18556+0136
G43.8−0.13	19 11 54.01	+09 35 50.52	37.5	11.8 [11]	IRAS 19095+0930
G107.30+5.64	22 21 27.61	+63 51 45.30	−7.1	0.76 [12]	IRAS 22198+6336, WB 176, L1204A

in the accretion of matter, can stimulate powerful maser flares (see, e.g., [3]). Strong variability of the source emission may testify that the region in which this radiation is formed is fairly compact. Such events make it possible to study such sources with high angular resolution, for example, using the RadioAstron ground–space interferometer [4, 5], since the probability of detecting the correlated signals (so-called “fringes”) increases appreciably when the source is very compact (in this case, an H₂O maser).

We present here the results of observations of H₂O maser sources in several regions of massive-star formation. We selected sources with H₂O maser flux densities of no less than 200 Jy over a prolonged period for this program (see Table 1). This threshold was chosen based on the sensitivities of very long baseline interferometers at 22 GHz (especially RadioAstron), which play an important role in studies of fine spatial structures.

2. DESCRIPTION OF THE SAMPLE SOURCES

In this section, we give a general description of the activity of the regions considered at various wavelengths. Information about the H₂O maser emission is presented in Section 5.

G25.65+1.05. This is a well studied star-forming region in which the massive young stellar object RAFGL 7009S [13] is embedded in an ultracompact HII region [14]. It is associated with a powerful bipolar outflow (see [15] and references therein). OH maser lines [16, 17] and Class I and II methanol maser lines (see [18] and references therein) are observed in this region. According to observations of the Class II methanol lines, the maser spots are probably organized in a disk structure [19].

G25.825−0.178. This source is associated with an ultracompact HII region [7] and a dense molecular core manifest at millimeter wavelengths [20]. Thermal emission from C₂H₃N, CH₃CN, and H₂CO [21, 22] molecules, as well as OH masers [23] and Class I [24] and Class II [25] methanol masers, have been detected in the direction of this source, which is identified with the short-wavelength infrared object SDC025.824−0.178.

G27.184−0.082. This source is associated with an ultracompact HII region [26], a dense molecular core manifest at millimeter wavelengths [20], and the short-wavelength infrared source SDC027.178−0.104. No information about Class I methanol masers is available, and no Class II methanol maser emission has been detected [27]. An OH maser was observed in [28]. Thermal emission from CS [29], HCO⁺, and N₂H⁺ molecules [30] has been observed.

G34.403+0.233. This source is an “Extended Green Object” (EGO) discovered by the Spitzer Space Observatory [31], distinguished by the presence of excess emission at 4.5 μm, indicating the presence of ionized or shock-compressed gas in the region. Both Class I and Class II methanol maser emission was detected in [18]. VLA observations displayed weak emission in all four lines of the main OH state [24].

G35.20−0.74. This is another EGO, in which a butterfly-shaped nebula and bipolar outflow oriented North–South are present [15]. Class II (from the VLBI observations of [32]) and Class I [33] methanol emission have been detected. OH maser emission is observed only in the main lines [24].

G43.8−0.13. This source is associated with an ultracompact HII region [14] and a bipolar outflow in CO [34], as well as OH [35] and Class II methanol [25] masers. It is identified with the short-wavelength infrared object SDC43.820−0.121.

G107.30+5.64. An ultracompact HII region is also observed in the direction of this source [36]. It is associated with a CO molecular outflow, a possible disk structure observed at 7 mm with the VLA, and a radio jet observed with the VLA at 1.3 cm (see [37] and references therein). No OH maser or Class I methanol maser emission has been detected [18]. Class II methanol maser has been observed in [61].

3. OBSERVATIONS

Our observations were carried out on the 22-m radio telescope of the Crimean Astrophysical Observatory of the Russian Academy of Sciences (CrAO, Simeiz). The height above sea level was 26.2 m, and the coordinates of the station are $44^{\circ}23'52.584''$ latitude and $33^{\circ}58'46.668''$ longitude.

The effective area of this 22-m antenna at 1.35 cm is 220 m^2 . For a point source, an antenna temperature of 1 K corresponds to a flux density of 13.6 Jy. The feed was mounted at the secondary focus of the radio telescope. The half-power beam width of the antenna at 22 GHz is $2.52' \pm 0.01'$. The width of the main lobe and the effective area of the radio telescope are essentially independent of the telescope orientation, as was confirmed earlier through a series of calibration observations [38]. The pointing of the antenna had an accuracy no worse than $2.5''$. This accuracy was realized by carefully taking into account systematic pointing errors, which were determined using observations at the shortest wavelengths (3, 4, and 8 mm), corresponding to the narrowest antenna beams for the radio telescope.

The telescope was equipped with a two-channel receiver operating in the range 22.0–22.6 GHz with a wide bandwidth of 100–600 MHz. The receiver was an uncooled High Electron Mobility Transistor (HEMT) with a noise temperature of 45 K. The signal can be recorded in either one circular or one linear polarization; the observations considered here were recorded in right-circular polarization. The signal was calibrated using a noise diode. The main heterodyne at a fixed frequency of 21 900 MHz was synchronized by a high-stability 5 MHz signal from a quartz or hydrogen frequency standard.

The typical system noise temperature was $T_{\text{sys}} = 150 \text{ K}$. The increase in the system temperature at elevations lower than 30° above the horizon due to the increased optical depth of the Earth's atmosphere was monitored during the observations using the atmosphere-section method. This is a standard method that consists of recording the intensity of the atmospheric emission at 22.2 GHz at elevations from 30° to 10° at a fixed azimuth.

The sources DR 21, NGC 7027, and 3C 274 were used as flux calibrators, with one of these observed at

the beginning of each hour. The target sources were observed over 30 minutes (12 scans of 2.5 min each). The uncertainty in the flux densities was no greater than 10%, and was due primarily to weather conditions and imperfect knowledge of the atmospheric absorption.

A universal parallel-type Fourier spectroanalyzer with an Athlon 1000 processor, consisting of a personal computer with an Athlon 1-GHz processor, two interface cards, and an analog–digital converter board, is used for observations with the CrAO 22-m telescope. The total bandwidth of the spectrometer can be set to 125, 256, 512 kHz or 1, 2, 4, 8 MHz, and the number of channels to 512, 2048, or 8192. During our observations, the spectrometer bandwidth was 4 MHz and the number of channels was 512, corresponding to a frequency resolution of 8 kHz and a velocity resolution of 0.108 km/s. The frequencies in the channels changed from observation to observation, depending on the source coordinates, radial velocity V_{LSR} , and observing date. The translation of the frequencies into radial velocities was carried out using a special program created by CrAO staff especially for the CrAO 22-m telescope. This program was tested by comparing its output results with known information for reference sources; it takes into account the observatory coordinates and all known motions (rotation of the Earth, motion of the Earth around the Sun, etc.).

Five cycles of observations of the seven maser sources in Table 1 were carried out from April 25–September 7, 2017, at the rest frequency for the H_2O transition, 22 235.07985 MHz. The observing dates were April 25, May 26, June 13, July 24, and September 7, 2017.

4. RESULTS

Emission from the sources was detected in all the observing sessions.

The data were reduced in the Continuum and Line Analysis Single-dish Software (CLASS) package created at the Institut de Radioastronomie Millimétrique (IRAM) in Grenoble (France), especially for the reduction of single-dish spectral data. The main steps in the processing of the spectral data included loading the raw data into CLASS using the *greg* procedure, subtracting the baseline level from each spectrum using the task *base*, and approximating each spectral line with a Gaussian function using the task *mini*.

The results of this processing are presented in Table 2 together with the parameters of the maser lines in the source spectra derived from the Gaussian line fitting. The names and coordinates of the sources are given in Table 2 in the J2000 system.

Table 2. Parameters of spectral data

Date	No.	$\int F_\nu \Delta V$	V_{LSR}	ΔV	F_ν^{peak}
G25.65+1.05 (18^h34^m20.96^s, −05°59′42.15″), J2000					
April 25, 2017	1	52.1 (10.6)	39.10 (0.05)	0.46 (0.10)	106.6
	2	646.3 (34.2)	41.65 (0.02)	0.83 (0.06)	730.6
	3	122.3 (20.2)	49.13 (0.14)	1.64 (0.30)	70.0
	4	223.2 (71.5)	53.03 (0.04)	0.52 (0.12)	404.1
	5	483.5 (102.4)	53.85 (0.19)	1.78 (0.34)	255.2
	6	87.8 (19.8)	57.50 (0.11)	1.14 (0.39)	72.7
May 26, 2017	1	104.4 (17.4)	37.18 (0.06)	0.80 (0.18)	122.0
	2	901.8 (15.4)	41.45 (0.02)	1.87 (0.04)	452.1
	3	167.0 (18.8)	48.58 (0.05)	0.96 (0.10)	163.3
	4	162.8 (24.3)	50.34 (0.11)	1.62 (0.30)	94.5
	5	762.0 (14.7)	53.53 (0.01)	1.55 (0.04)	461.6
June 13, 2017	1	86.2 (10.2)	37.45 (0.04)	0.68 (0.09)	118.5
	2	362.4 (41.7)	41.15 (0.06)	1.16 (0.10)	293.9
	3	489.5 (41.9)	42.47 (0.05)	1.24 (0.09)	372.0
	4	55.3 (9.6)	48.94 (0.06)	0.64 (0.11)	81.1
	5	414.6 (15.4)	50.88 (0.02)	1.29 (0.06)	301.5
	6	55.2 (50.6)	52.64 (0.57)	1.02 (0.75)	51.1
	7	539.7 (12.5)	53.97 (0.01)	0.91 (0.03)	555.7
July 24, 2017	1	179.7 (12.8)	37.07 (0.02)	0.70 (0.06)	243.0
	2	206.2 (29.1)	40.99 (0.04)	0.76 (0.08)	254.3
	3	596.4 (33.0)	42.20 (0.03)	1.29 (0.08)	435.5
	4	73.0 (18.4)	48.83 (0.18)	1.26 (0.43)	54.4
	5	215.3 (88.2)	52.02 (0.03)	0.92 (0.21)	220.5
	6	447.5 (104.4)	53.11 (0.30)	2.53 (0.33)	166.0
September 7, 2017	1	284.9 (13.4)	37.04 (0.02)	0.65 (0.03)	411.2
	2	15410.0 (78.5)	42.78 (0.01)	0.86 (0.01)	16841.0
	3	221.1 (27.5)	51.34 (0.05)	0.87 (0.11)	238.8
	4	416.0 (38.0)	52.39 (0.02)	0.81 (0.07)	482.1
	5	132.4 (24.1)	53.52 (0.10)	1.01 (0.18)	122.7
G25.825−0.178 (18^h39^m03.60^s, −06°24′11.17″), J2000					
April 25, 2017	1	336.5 (21.3)	80.80 (0.08)	2.40 (0.18)	131.6
	2	182.8 (15.6)	84.78 (0.06)	1.41 (0.13)	122.2
	3	115.6 (18.1)	89.62 (0.04)	0.58 (0.09)	185.8
	4	69.5 (20.4)	90.58 (0.17)	0.99 (0.26)	65.7
	5	531.2 (26.8)	92.81 (0.05)	2.30 (0.16)	216.9
May 26, 2017	1	188.3 (26.3)	79.63 (0.07)	1.22 (0.19)	145.3
	2	264.7 (24.1)	81.11 (0.05)	1.17 (0.11)	213.5
	3	465.7 (13.8)	84.38 (0.02)	1.41 (0.05)	310.8
	4	271.8 (14.5)	89.69 (0.03)	1.14 (0.09)	223.3
	5	379.2 (18.0)	92.68 (0.04)	1.77 (0.12)	200.9

Table 2. (Contd.)

Date	No.	$\int F_\nu \Delta V$	V_{LSR}	ΔV	F_ν^{peak}
June 13, 2017	1	205.9 (23.9)	79.45 (0.06)	1.27 (0.14)	152.7
	2	253.9 (24.0)	80.95 (0.05)	1.27 (0.12)	187.6
	3	589.9 (12.2)	84.25 (0.02)	1.57 (0.04)	353.5
	4	335.2 (10.5)	89.57 (0.01)	0.97 (0.04)	325.1
	5	318.4 (14.7)	92.26 (0.03)	1.23 (0.07)	243.0
July 24, 2017	1	229.9 (12.5)	78.91 (0.03)	1.21 (0.08)	178.4
	2	177.8 (13.0)	80.89 (0.04)	1.34 (0.12)	124.5
	3	337.5 (12.3)	84.23 (0.04)	1.95 (0.08)	163.0
	4	374.2 (40.2)	89.49 (0.05)	1.40 (0.09)	251.5
	5	390.6 (42.3)	91.46 (0.12)	2.38 (0.26)	154.3
September 7, 2017	1	370.6 (24.5)	79.50 (0.05)	1.49 (0.13)	233.9
	2	301.5 (85.8)	85.02 (0.20)	1.45 (0.31)	195.8
	3	402.1 (81.4)	86.00 (0.04)	0.91 (0.07)	416.0
	4	391.2 (26.7)	82.10 (0.05)	1.66 (0.15)	222.1
	5	1719.6 (75.5)	91.11 (0.04)	1.96 (0.07)	825.6
	6	692.8 (75.9)	93.02 (0.07)	1.74 (0.14)	374.7
G27.184−0.082 (18 ^h 41 ^m 13.21 ^s , −05°09′05.13″), J2000					
April 25, 2017	1	78.6 (20.7)	16.23 (0.09)	0.73 (0.15)	101.3
	2	563.8 (77.9)	17.95 (0.08)	1.59 (0.23)	332.8
	3	840.3 (65.3)	19.30 (0.02)	0.99 (0.05)	799.4
	4	395.3 (45.8)	26.78 (0.10)	2.17 (0.28)	171.5
	5	241.4 (43.1)	29.32 (0.13)	1.79 (0.35)	126.7
May 26, 2017	1	1015.4 (35.1)	18.53 (0.04)	2.55 (0.08)	374.6
	2	351.4 (21.7)	19.32 (0.01)	0.63 (0.03)	520.6
	3	98.2 (21.6)	21.34 (0.13)	1.29 (0.36)	71.3
	4	673.4 (19.2)	27.20 (0.02)	1.67 (0.06)	378.5
June 13, 2017	1	151.1 (12.2)	15.40 (0.04)	0.92 (0.08)	154.9
	2	613.5 (37.8)	17.83 (0.05)	1.86 (0.12)	310.0
	3	519.8 (30.3)	19.20 (0.01)	0.82 (0.03)	595.1
	4	32.4 (10.0)	20.60 (0.14)	0.80 (0.23)	38.1
July 24, 2017	1	76.5 (28.6)	15.52 (0.14)	1.06 (0.28)	67.8
	2	520.8 (55.1)	17.38 (0.05)	1.89 (0.24)	258.4
	3	500.7 (35.3)	19.19 (0.02)	1.03 (0.06)	458.8
	4	277.6 (30.5)	27.04 (0.29)	5.54 (0.76)	47.1
September 7, 2017	1	749.2 (35.3)	17.45 (0.04)	1.96 (0.11)	358.7
	2	405.6 (30.9)	19.35 (0.03)	1.08 (0.08)	353.5
G34.403+0.233 (18 ^h 53 ^m 18.00 ^s , +01°25′26.00″), J2000					
April 25, 2017	1	71.9 (17.2)	50.54 (0.25)	1.56 (0.41)	43.4
	2	111.5 (49.2)	52.92 (0.20)	1.40 (0.73)	74.7
	3	571.0 (18.9)	54.24 (0.01)	0.74 (0.02)	725.0
	4	723.1 (43.0)	55.04 (0.11)	3.42 (0.26)	198.5
	5	575.9 (19.0)	56.53 (0.01)	0.60 (0.02)	910.0
	6	468.7 (20.5)	58.09 (0.01)	0.80 (0.03)	550.5
	7	223.6 (14.6)	59.45 (0.03)	1.03 (0.08)	204.9
	8	28.7 (8.3)	77.35 (0.08)	0.58 (0.19)	46.8

Table 2. (Contd.)

Date	No.	$\int F_{\nu} \Delta V$	V_{LSR}	ΔV	F_{ν}^{peak}
May 26, 2017	1	131.8 (22.7)	50.65 (0.15)	1.90 (0.43)	65.2
	2	170.4 (19.3)	52.68 (0.04)	0.94 (0.12)	170.4
	3	225.2 (56.4)	54.12 (0.03)	0.76 (0.11)	280.0
	4	831.6 (59.2)	54.78 (0.08)	1.98 (0.10)	395.2
	5	830.8 (19.1)	56.58 (0.01)	0.65 (0.01)	1204.7
	6	305.6 (24.1)	58.13 (0.03)	1.01 (0.08)	283.2
	7	274.6 (27.1)	59.60 (0.05)	1.25 (0.15)	205.8
June 13, 2017	1	435.8 (53.0)	53.82 (0.02)	0.74 (0.05)	557.0
	2	603.2 (75.8)	55.03 (0.05)	1.50 (0.23)	378.1
	3	932.6 (28.2)	56.55 (0.01)	0.75 (0.03)	1170.7
	4	596.0 (36.2)	58.04 (0.03)	0.82 (0.06)	680.3
	5	298.4 (41.6)	59.50 (0.07)	1.12 (0.20)	251.0
July 24, 2017	1	111.3 (16.2)	52.10 (0.09)	1.27 (0.23)	82.2
	2	588.0 (94.3)	54.29 (0.10)	1.56 (0.16)	353.7
	3	352.8 (76.6)	56.08 (0.29)	1.74 (0.44)	190.6
	4	358.2 (40.7)	56.62 (0.01)	0.57 (0.04)	587.5
	5	347.9 (16.7)	58.18 (0.02)	0.86 (0.05)	381.5
	6	251.1 (17.2)	59.59 (0.04)	1.19 (0.10)	197.6
September 7, 2017	1	151.1 (27.8)	51.16 (0.11)	1.46 (0.42)	97.4
	2	250.6 (62.6)	53.97 (0.09)	1.03 (0.13)	228.2
	3	310.0 (76.8)	55.18 (0.09)	1.29 (0.31)	225.3
	4	742.0 (18.5)	56.59 (0.01)	0.81 (0.03)	856.1
	5	101.3 (17.3)	57.93 (0.06)	0.61 (0.09)	157.0
	6	61.0 (35.9)	58.54 (0.07)	0.53 (0.27)	108.8
	7	237.2 (32.6)	59.43 (0.07)	0.98 (0.15)	228.5
G35.20−0.74 (18 ^h 58 ^m 13.21 ^s , +01°40′35.29″), J2000					
April 25, 2017	1	164.5 (27.3)	29.74 (0.06)	1.09 (0.26)	142.4
	2	90.1 (19.1)	30.91 (0.07)	0.73 (0.11)	116.7
May 26, 2017	1	277.4 (12.6)	30.03 (0.05)	2.42 (0.13)	107.8
June 13, 2017	1	336.0 (15.6)	29.76 (0.05)	2.17 (0.12)	145.8
July 24, 2017	1	393.9 (16.2)	30.19 (0.04)	1.84 (0.09)	201.0
September 7, 2017	1	344.7 (124.9)	29.94 (0.38)	2.21 (0.45)	146.4
	2	241.7 (36.8)	30.18 (0.01)	0.48 (0.04)	474.5
	3	107.0 (36.3)	30.84 (0.03)	0.39 (0.06)	258.5
	4	299.1 (50.4)	31.50 (0.02)	0.62 (0.06)	453.2
G43.8−0.13 (19 ^h 11 ^m 54.01 ^s , +09°35′50.52″), J2000					
April 25, 2017	1	778.2 (14.9)	37.67 (0.01)	0.51 (0.01)	1444.2
	2	178.1 (18.7)	38.54 (0.03)	0.66 (0.08)	255.6
	3	426.1 (23.9)	40.36 (0.04)	1.54 (0.11)	259.7
May 26, 2017	1	637.4 (8.8)	37.7 (0.01)	0.52 (0.01)	1160.2
	2	128.2 (8.9)	38.58 (0.02)	0.55 (0.05)	217.0
	3	243.3 (28.9)	40.35 (0.03)	1.27 (0.10)	179.4
	4	250.8 (55.3)	40.70 (0.52)	5.40 (0.76)	43.6

Table 2. (Contd.)

Date	No.	$\int F_\nu \Delta V$	V_{LSR}	ΔV	F_ν^{peak}
June 13, 2017	1	1291.4 (8.6)	37.60 (0.01)	0.52 (0.01)	2331.7
	2	259.3 (9.5)	38.44 (0.01)	0.52 (0.02)	465.2
	3	710.7 (18.5)	40.15 (0.02)	1.44 (0.04)	462.7
	4	77.6 (9.8)	40.68 (0.01)	0.31 (0.03)	235.6
	5	218.3 (50.8)	41.91 (0.10)	1.72 (0.46)	119.5
	6	149.3 (35.5)	43.49 (0.09)	1.09 (0.16)	128.3
July 24, 2017	1	710.5 (11.8)	37.74 (0.01)	0.52 (0.01)	1283.4
	2	162.1 (13.6)	38.64 (0.03)	0.70 (0.07)	218.8
	3	515.1 (23.8)	40.33 (0.03)	1.44 (0.07)	337.0
	4	66.5 (13.9)	40.78 (0.02)	0.34 (0.05)	185.1
	5	146.4 (26.0)	42.18 (0.17)	2.03 (0.4)	67.6
September 7, 2017	1	94.7 (8.7)	34.66 (0.04)	0.93 (0.10)	95.6
	2	220.2 (11.0)	37.77 (0.01)	0.64 (0.05)	321.5
	3	153.7 (35.4)	38.18 (0.21)	1.80 (0.34)	80.2
	4	152.3 (47.1)	39.99 (0.13)	0.95 (0.29)	150.6
	5	91.0 (43.4)	40.75 (0.07)	0.56 (0.15)	153.5
G107.30+5.64 (22 ^h 21 ^m 27.61 ^s , +63°51′45.30″), J2000					
April 25, 2017	1	138.3 (23.8)	−17.04 (0.03)	0.61 (0.06)	212.8
	2	497.6 (35.2)	−16.26 (0.07)	2.07 (0.13)	226.4
	3	84.9 (16.0)	−7.32 (0.10)	1.05 (0.26)	76.0
May 26, 2017	1	72.4 (7.2)	−19.23 (0.02)	0.45 (0.05)	152.5
	2	707.1 (14.4)	−17.03 (0.02)	1.71 (0.04)	388.3
	3	63.6 (10.3)	−7.73 (0.10)	1.11 (0.19)	53.8
June 13, 2017	1	475.2 (16.7)	−17.30 (0.03)	1.64 (0.07)	272.1
	2	84.9 (15.2)	−8.11 (0.13)	1.42 (0.30)	56.2
July 24, 2017	1	58.5 (5.9)	−19.88 (0.03)	0.59 (0.06)	93.6
	2	196.3 (8.1)	−17.38 (0.02)	1.00 (0.05)	185.2
	3	24.6 (5.5)	−8.71 (0.07)	0.56 (0.12)	41.6
September 7, 2017	1	122.2 (16.2)	−19.62 (0.04)	0.64 (0.10)	180.9
	2	369.8 (41.7)	−17.65 (0.07)	1.40 (0.20)	248.2

The columns in Table 2 give (1) the observing date, (2) ordinal numbers for the spectral components in order of increasing velocity for the peak, (3)–(6) the fitting results for the components and the associated uncertainties—the integrated flux $\int F_\nu \Delta V$, radial velocity at the line peak V_{LSR} , line full width at half maximum ΔV , and peak flux density F_ν^{peak} (amplitude). The source spectra are presented in Figs. 1–7, where the horizontal axis plots the radial velocity

V_{LSR} and the vertical axis the flux density F_ν in Jy. The observing date is indicated on each spectrum.

In addition to the spectra obtained on the CrAO 22-m telescope, for comparison, we also considered unpublished spectra obtained earlier on the 22-m telescope of the Pushchino Radio Astronomy Observatory (PRAO) during this same period (see Figs. 8–14).

Figure 15 shows for each source the dependence of the total flux density in all spectral lines (upper

panels) and the flux density of the highest peak in the spectrum (lower panels) on the observing date. These plots visually illustrate the character of the source variability over the five months of observations, and are considered in more detail in Section 6.

5. COMMENTS AND COMPARISON WITH OTHER OBSERVATIONS

5.1. G25.65+1.05

The H₂O maser in this source has been observed over a long period since 1989 [36, 39]. One bright maser feature with a flux density of 720 Jy at a velocity of $V_{\text{peak}} = 45.2$ km/s was initially detected. A spectrum obtained on the 100-m Effelsberg telescope in 1995 [40] differed from the previous spectrum: two features were present—a new (“blue”) feature at $V_{\text{LSR}} = 41.2$ km/s with a peak flux density of 450 Jy and the formerly detected (“red”) feature at $V_{\text{LSR}} = 45.2$ km/s with a flux density of 250 Jy.

G25.65+1.05 (further G25.65) was monitored on the PRAO 22-m telescope starting from 2002 [41]. A powerful maser flare was detected in November–December 2016, reaching 40 000 Jy on December 12, 2016 [42]. The flaring feature had a velocity of 41.8 km/s, which differs from the velocity of the feature observed in 1995 by 0.6 km/s. Subsequent monitoring of G25.65 on the PRAO 22-m antenna showed that the flare was already decaying by January 2017, when the peak flux density was 6000 Jy, with the flux density dropping to 160 Jy in February–March 2017. Figure 8 presents the spectrum of G25.65 obtained on the PRAO 22-m antenna in May–July 2017.

Monitoring of G25.65 on the CrAO 22-m telescope in Simeiz began in April 2017 (see Fig. 1). Three groups of features are observed in the spectrum: one at ~ 37 km/s, a second at 40–43 km/s, and a third at 50–54 km/s. The group of features at ~ 37 km/s is present in all the spectra apart from one obtained on April 25, 2017; features appear at velocities of 36.7–37.4 km/s, with the flux densities of some of them growing from 120 to 410 Jy during the period covered by the observations.

The second group of features underwent appreciable variations during the five months of observations. At the beginning of the observations, on April 25, 2017, a bright maser line with a peak flux density of 820 Jy is present at a velocity of 41.3 km/s, and a group of from one to three features with flux densities of 400–500 Jy is present at velocities of 40–43 km/s a month later. This group of lines remained in the same ranges of flux density and velocity over the next two

months of observations (June–July 2017). A powerful flare of the maser emission to 17 000 Jy at the line peak at a velocity of about 42.8 km/s was observed in September 2017. After receiving information about this flare, we organized interferometric observations of the source with RadioAstron within a fairly short time. Thus, the main aim of our monitoring of maser sources with the CrAO 22-m telescope referred to in the Introduction was achieved: identifying sources suitable for observations with RadioAstron.

The third group of maser lines also varied fairly substantially during the five months of observations, with various features growing or decreasing in flux. For example, a feature with a velocity of 52.6 km/s and a flux density of 500 Jy that is present at the beginning of the observations is also present in September with the same velocity and flux density. In the interval between these epochs, features at velocities of 51 and 53–54 km/s varying in flux density from 100 to 400 Jy are present.

5.2. G25.825–0.178

This source (further G25.825) was observed in 2010 as part of the 22-GHz HOPS survey on the 22-m Mopra telescope in Australia [43], when it had a flux density of 345 Jy at $V_{\text{peak}} = 91$ km/s. This emission was also accompanied by two weaker lines with peak flux densities of 165 Jy and 135 Jy at 85 and 93 km/s, respectively. The source was also observed with ATCA [44] in 2011–2012, when it had a flux density of 400 Jy at 91 km/s.

The maser G25.825 was observed on the PRAO 22-m telescope in November 2016. A comparison of the spectra obtained on the Mopra and PRAO 22-m telescopes showed that a new feature with a peak flux density of 400 Jy had appeared at 80 km/s and a feature at 85 km/s had virtually disappeared in the interval between these observations; the flux density of the brightest feature observed in 2010 at a velocity of $V_{\text{LSR}} = 91$ km/s had decreased by about a factor of five, to ~ 70 Jy. The line observed in the Mopra spectrum at $V_{\text{LSR}} = 93$ km/s was retained, and displayed a flux density increase to 280 Jy. The following observations of G25.825 at the PRAO in January 2017 showed that the spectrum had varied substantially over this relatively short time interval of less than two months. The flux density of the feature observed at $V_{\text{LSR}} = 80$ km/s decreased by a factor of four, to 100 Jy. The peak flux density at 91 km/s observed in 2010 became even weaker, no more than 50 Jy. The feature at $V_{\text{LSR}} = 93$ km/s remained relatively stable, slightly increasing its peak flux density from 280 to 320 Jy.

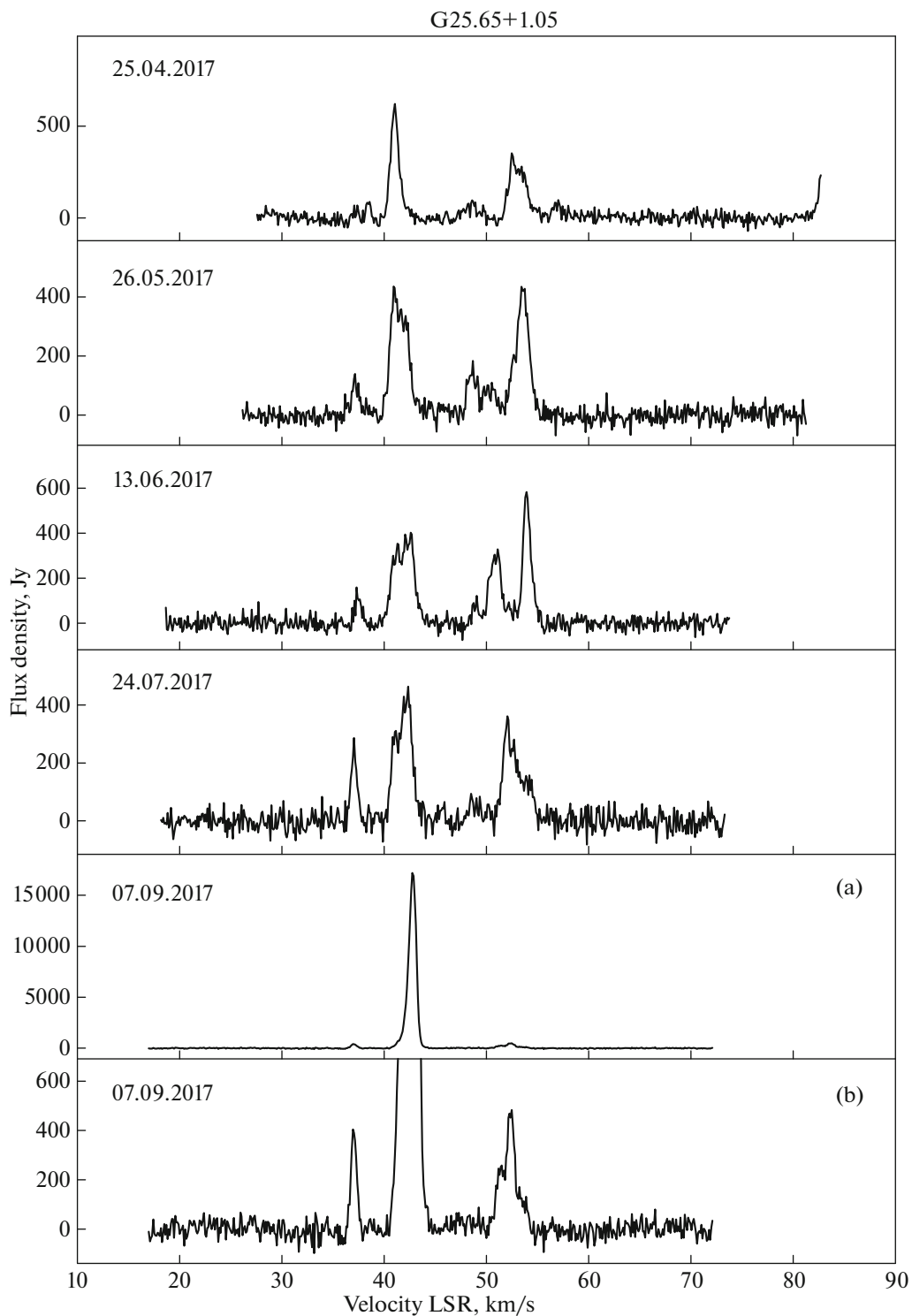


Fig. 1. Spectrum of G25.65+1.05 obtained in five observing sessions on the CrAO 22-m telescope from April 25–September 7, 2017.

Observations of G25.825 on the CrAO 22-m antenna began roughly three months after the PRAO observations (see Fig. 2). A comparison of the spectra for January 17, 2017 (PRAO) and April 25, 2017 (CrAO) shows an absence of dramatic variations dur-

ing this time interval. As previously, the line at 93 km/s remained stable, with a flux density of about 300 Jy. The feature at 90 km/s increased in flux to 220 Jy, by more than a factor of four. The feature at 85 km/s again grew to a flux density of 140 Jy, close

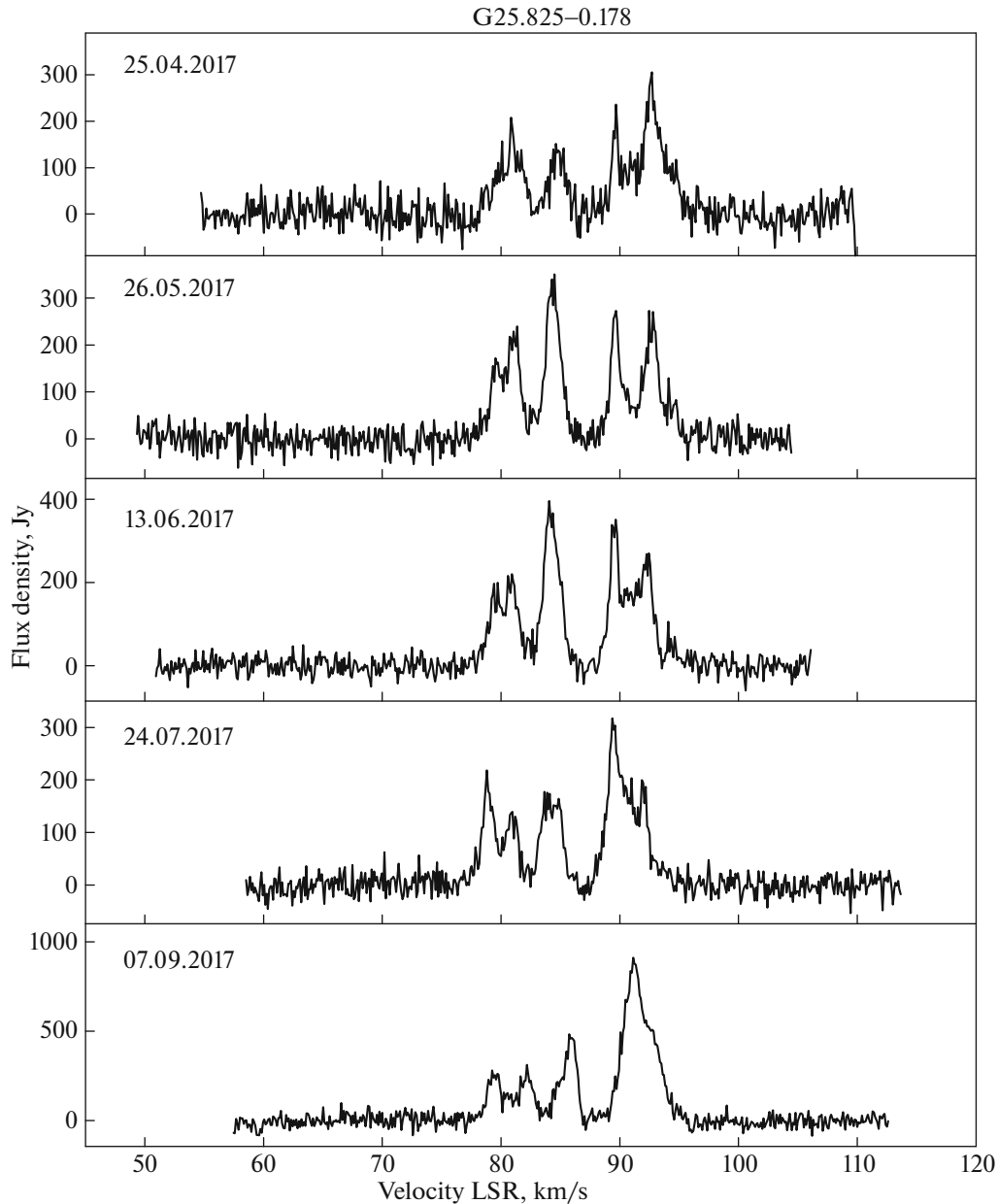


Fig. 2. Same as Fig. 1 for G25.825-0.178.

to its value in 2010. Over the next three observing sessions, the spectrum did not display any cardinal variations, with the flux densities of all the components varying within ~ 200 – 400 Jy (see Fig. 2). The spectrum for September 7, 2017 shows that the flux density of the feature at 91 km/s had increased to 900 Jy, a factor of three higher than at the earlier observing epochs, when its flux density was relatively stable at ~ 300 Jy. Moreover, the flux density of the neighboring feature at 93 km/s also increased by a factor of 2.5 compared to earlier observations, to 500 Jy. We can also note the appreciable increase in the flux density of the feature at 86 km/s to 500 Jy,

compared to the PRAO spectrum obtained on January 17, 2017, when it had a flux density of about 50 Jy, about a factor of 10 lower.

This source was also observed on the PRAO 22-m telescope in May–July (see Fig. 9). Overall, analysis of spectra for G25.825 from the literature and the 2017 observations indicates the presence of at least four to five features corresponding to various velocities in the range 80–95 km/s. The flux density in lines can vary by a factor of three to four, on average.

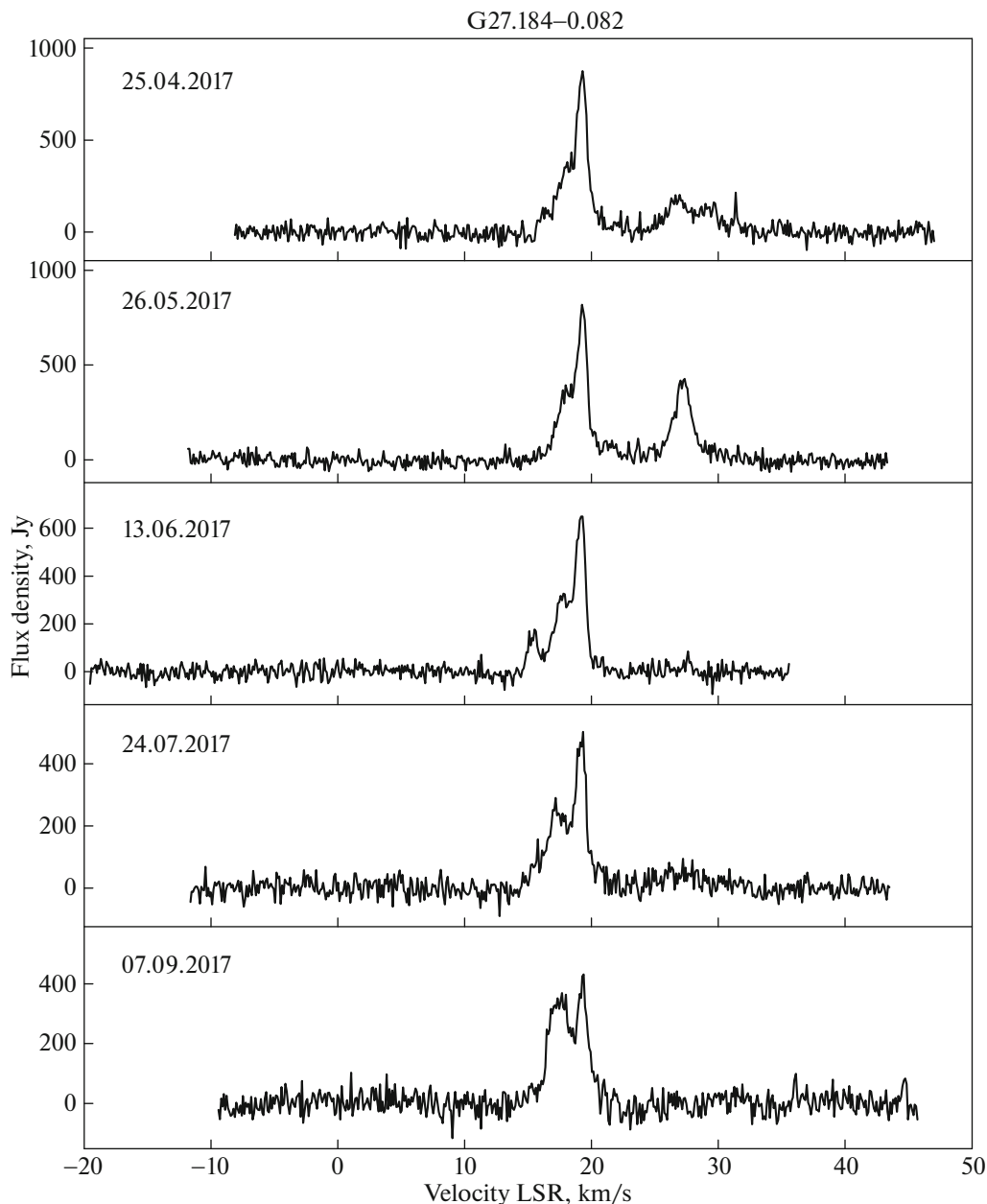


Fig. 3. Same as Fig. 1 for G27.184–0.082.

5.3. G27.184–0.082

The source G27.184–0.082 (further G27.184) was observed in 2010 on the Mopra 22-m telescope [43] as part of the HOPS survey, and in 2009–2010 on the 100-m Green Bank Telescope (GBT, USA) [45]. Several features were observed in the spectrum, the brightest of which had a peak flux density of 3500 Jy at $V_{\text{LSR}} = 17.5$ km/s. A fairly bright feature with a flux density of 600–1000 Jy is present at 14.5 km/s, and a bright line with a flux density varying from 400 Jy (Mopra) to 1400 Jy (GBT) is present at 20 km/s; i.e., this line may

display rapid variability (the observations on both telescopes were conducted over several months in the same year). Another feature with a flux density of about 200 Jy is also visible in the Mopra spectrum at a velocity of 30 km/s, which is not visible in the GBT spectrum. In ATCA observations obtained in 2011 [44], a feature with a flux density of 200 Jy was also detected at $V_{\text{LSR}} = 17.5$ km/s.

Observations with the PRAO 22-m telescope in 2016–2017 showed the presence of two features with flux densities of 200–300 Jy at velocities of 18.5–19 km/s and 29–30 km/s. Figure 10 presents spectra

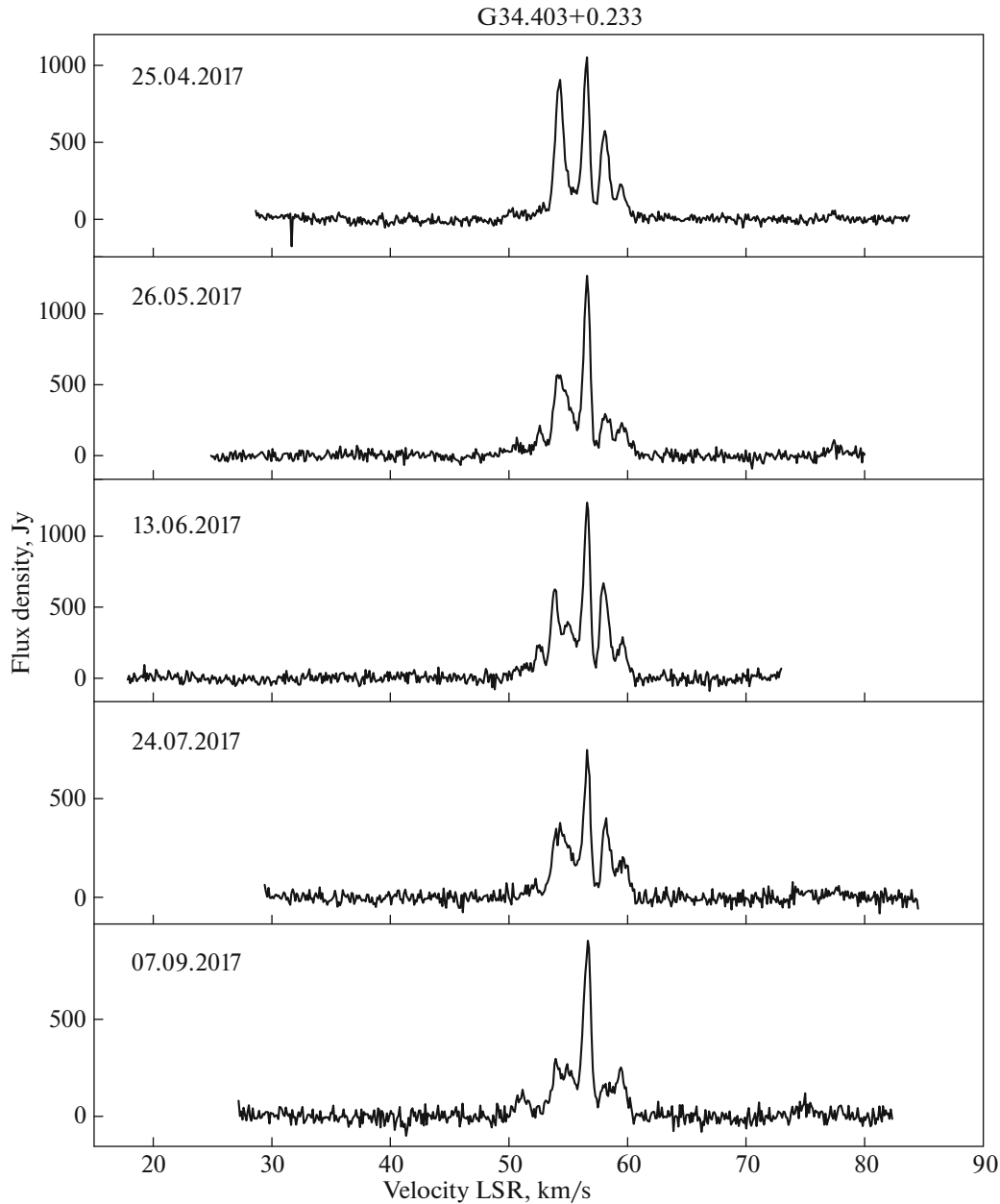


Fig. 4. Same as Fig. 1 for G34.403+0.233.

of G27.184 obtained on the PRAO 22-m telescope in May and June 2017.

During monitoring with the CrAO 22-m antenna from April through September, the brightest line continued to be present near 19 km/s, with its position varying within 0.5 km/s of this velocity (see Fig. 3). The peak flux density of this feature gradually decreased from 850 to 400 Jy over nearly five months. Several lines with flux densities from 200 Jy to 400 Jy are also present to the left of this line, whose positions in velocity vary from month to month. A feature with $V_{\text{LSR}} = 26.5$ km/s detected on April 25 with a flux

density of about 150 Jy had increased its flux density to 400 Jy a month later, after which it completely disappeared up to the end of the observations.

5.4. G34.403+0.233

Observations of this source (further G34.403) were carried out in 2008–2010 on the Nobeyama 45-m telescope (Japan) [46], which revealed the presence of several maser components. The brightest group of components was located at velocities from 45 to 63 km/s; the brightest maser line, with a peak flux

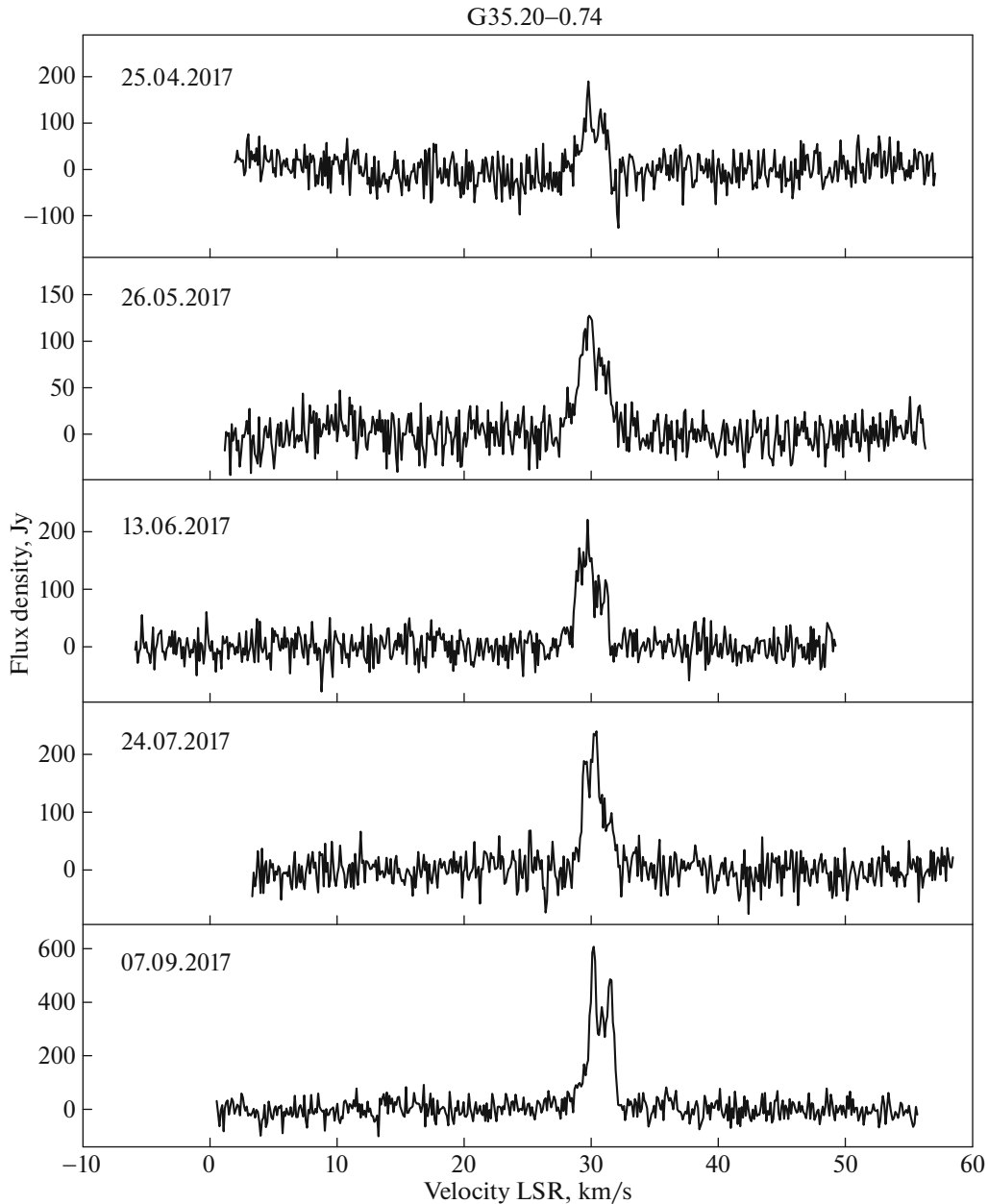


Fig. 5. Same as Fig. 1 for G35.20–0.74.

density of 220 Jy, was located at $V_{\text{LSR}} = 57$ km/s. Two more lines with $V_{\text{LSR}} = 53$ and 60 km/s and flux densities of 80 Jy and 60 Jy can also be distinguished in this group. In addition to this main group of maser features, two weak features (flux densities of less than 10 Jy) were also observed at the same epoch at velocities of ~ 18 and ~ 32 km/s, which were not subsequently detected; a group of lines near $V_{\text{LSR}} = 81$ km/s with flux densities of no more than 20 Jy was also observed, which was not subsequently detected in the observational period considered.

The strongest H_2O maser feature, with a flux

density of 1310 Jy at $V_{\text{peak}} = 54.50$ km/s, was detected on the VLA toward the cool molecular core IRDC MM1 [47]. Interferometric observations of G34.403 were also carried out earlier in 2006 using VERA [9]; the source was found to have a flux density of 60 Jy at 57 km/s on the fairly long Mizusawa–Iriki baseline (1300 km). Another feature with a flux density of about 27 Jy was observed at 38 km/s. Thus, it was shown that the H_2O emission is unresolved on long baselines [9]; the distribution of most of the maser spots was reported to have a V-shaped structure in [48]. It is possible that the same feature

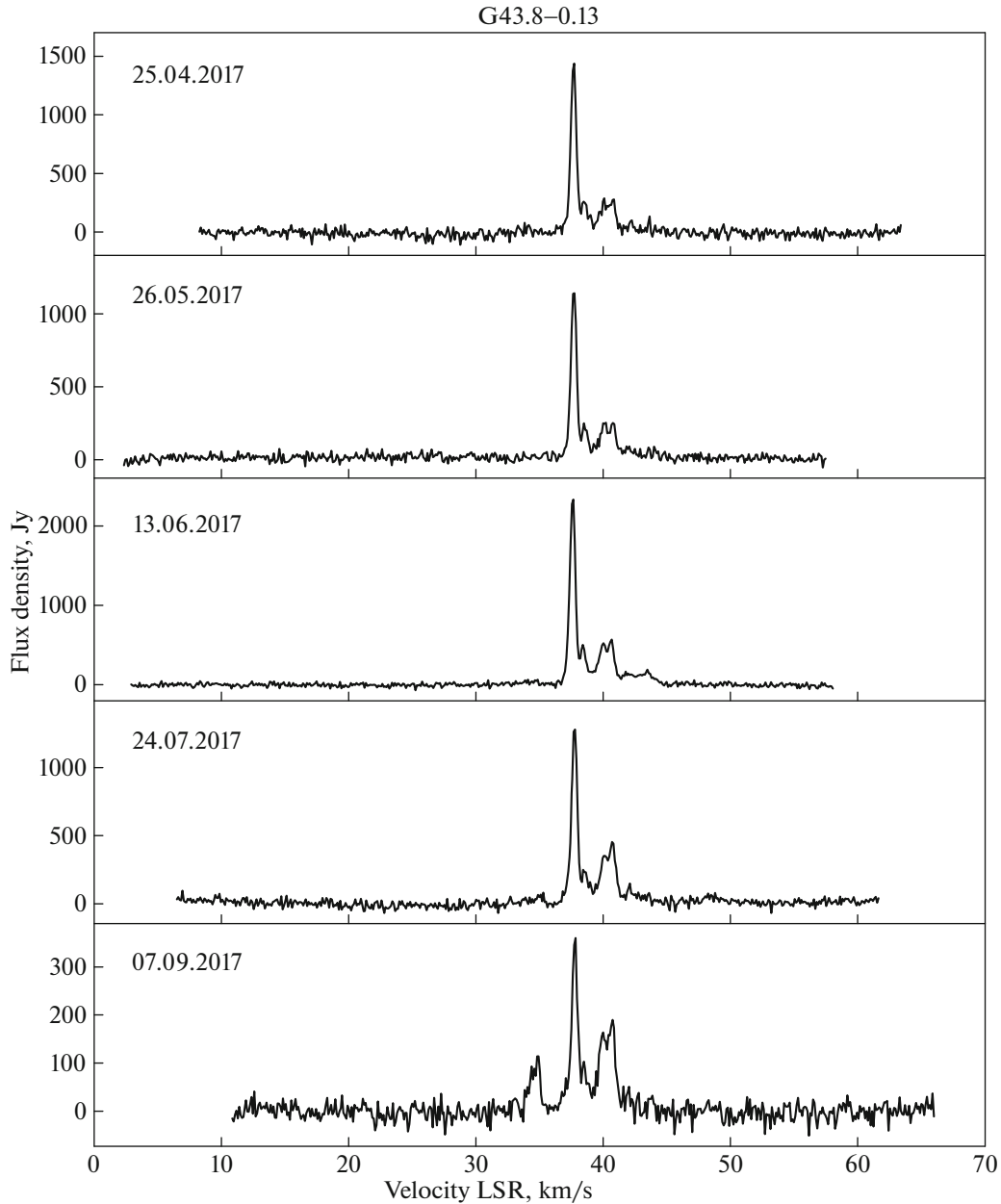


Fig. 6. Same as Fig. 1 for G43.8-0.13.

with $V_{\text{LSR}} = 57$ km/s observed in 2008–2010 with the Nobeyama 45-m telescope was observed in 2006, with the flux density staying the same during this period. This same feature remained in the spectrum of G34.403 over the entire period covered by the subsequent observations (see our analysis below). This suggests that the brightest feature at $V_{\text{LSR}} = 57$ km/s is not resolved on long baselines; i.e., it is fairly compact. Moreover, several other weaker features in this group of maser lines are also unresolved; i.e., this is a group of several compact maser spots.

We can estimate the size of the region from which the emission in a maser line arises based on data for

the mean flux density of the maser line in the single-dish spectrum and in the cross-correlation spectrum obtained with VERA. A method for estimating the brightness temperature and angular size of a radiating region for various cases of the brightness distribution as a function of the coordinates of this region projected on the celestial sphere is proposed in [49], in particular, for a Gaussian distribution. Using this method and assuming that the peak flux density in the line with $V_{\text{LSR}} = 57$ km/s is 220 Jy (see the spectrum of [46]), as is true closest to the VERA epoch, and also taking the flux density of this feature in the cross-correlation spectrum to be 60 Jy for a baseline length

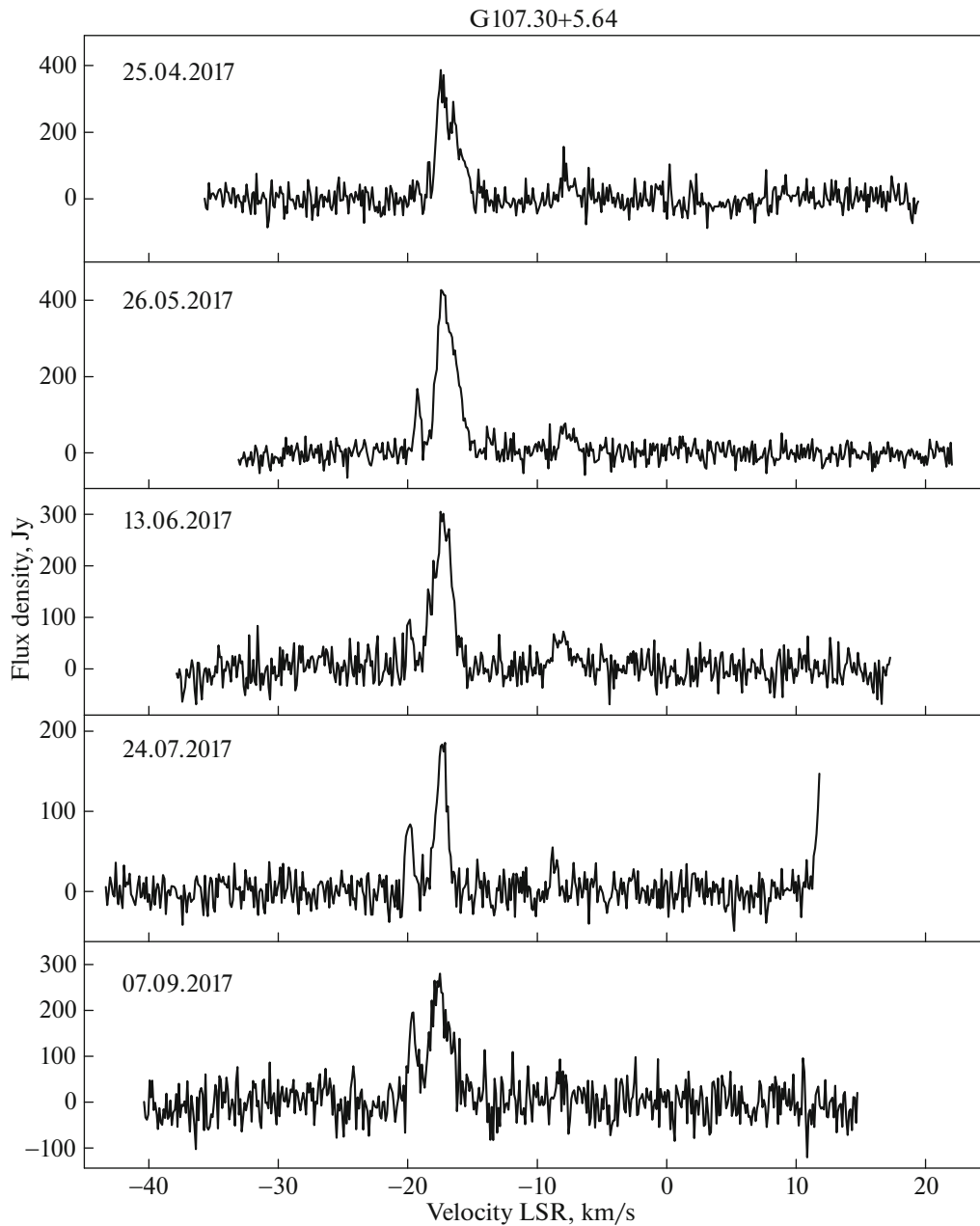


Fig. 7. Same as Fig. 1 for G107.30+5.64.

$B = 1300$ km, we obtained the upper limit for the angular size of the maser spot $\theta_1 = 1.3$ mas¹. The parallax and distance to G34.403 were found in [9] to be 0.643 mas and 1.56 kpc. At this distance, an angular size of 1.3 mas corresponds to a linear size of about 2 AU. For the indicated parameters, the source brightness temperature is $T_b = 3.3 \times 10^{11}$ K.

The source G34.403 was observed on the PRAO 22-m telescope in 2015–2016 [50]. The line at

¹mas refers to a milliarcsecond; the units of measurement of proper motion are mas/year.

$V_{\text{LSR}} = 57$ km/s had a peak flux density of 350–450 Jy in 2015, which rose to 1000 Jy at the end of 2016. Simultaneously, a feature with a peak flux density of 1200 Jy appeared in the spectrum at a velocity of 54.5 km/s, which had not been observed before. Two months later, in January 2017, both of these lines had flux densities of about 1000 Jy. Figure 11 presents spectra of G34.403 obtained on the PRAO 22-m telescope in May–July 2017.

Observations of this source on the CrAO 22-m telescope began on April 25; these spectra are presented in Fig. 4. During the period covered by

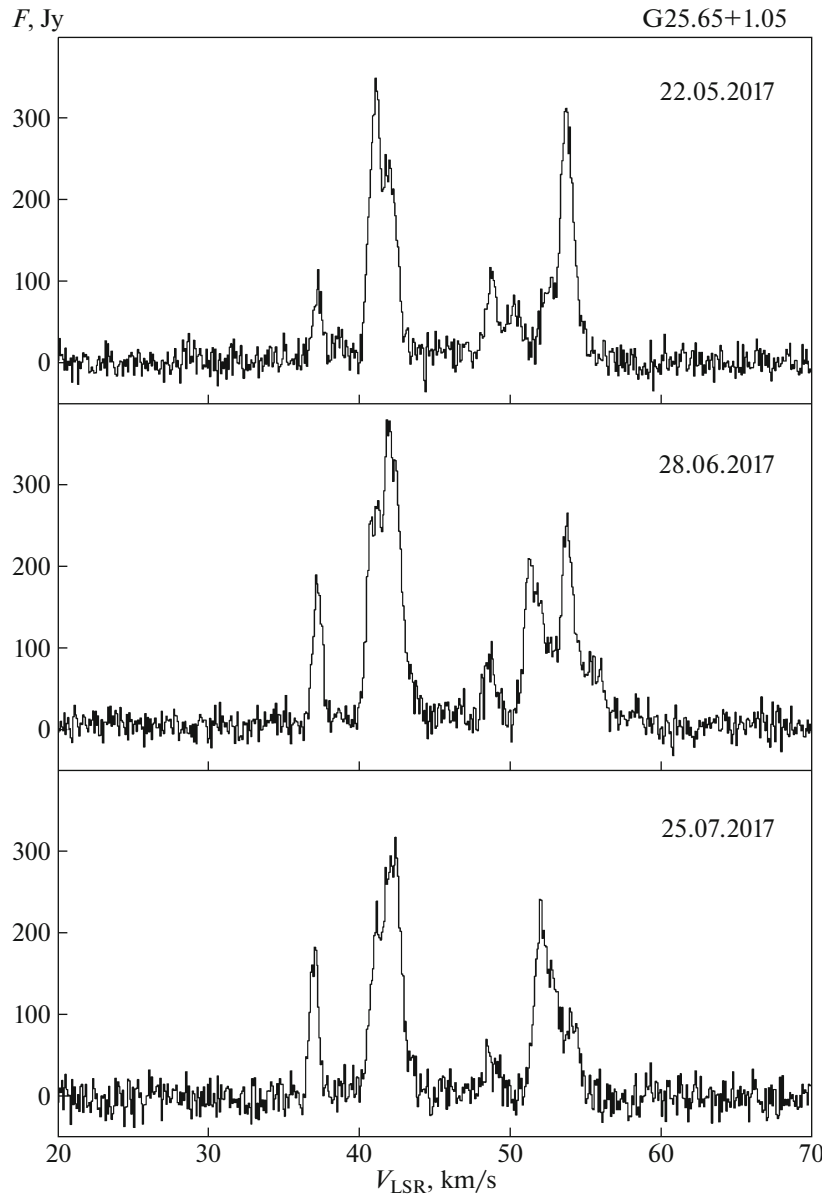


Fig. 8. Spectra of G25.65+1.05 obtained on the PRAO 22-m telescope in 2017.

the CrAO observations (five months), the feature at 57 km/s (which we will call the “main” feature) had a mean flux density of 1000 Jy, varying in the range 800–1300 Jy. The new feature at 54.5 km/s gradually decreased in flux density from 900 Jy in April 2017 to 300 Jy in September 2017. In addition to these two lines, two weaker features with mean flux densities of 400 and 250 Jy at velocities of $V_{\text{LSR}} = 58$ and 60 km/s were also present in the spectrum of G34.403.

5.5. G35.20–0.74

Two H₂O masers are present in the northern and southern parts of the G35.20–0.74 molecular cloud

(further G35.20) [51]; we observed the emission from the northern H₂O masers, which are believed to be in an earlier stage of their evolution than the southern masers. The source was monitored using the 32-m Medicina telescope (Italy) from 1987–2007 [52, 53]. During this period, the source displayed variability of all its components, reaching a maximum flux density of 340 Jy at a velocity of about 32 km/s. On average, the source brightness over 20 years was about 40 Jy, and the integrated flux from all its components grew monotonically starting roughly from 2000, with three well-defined peaks of activity in 1994, 2002, and 2006 (see [52, Figs. A.24.d and A.24.e]).

Observations of G35.20 on the Nobeyama 45-m telescope were carried out in 2008–2010 [46], when

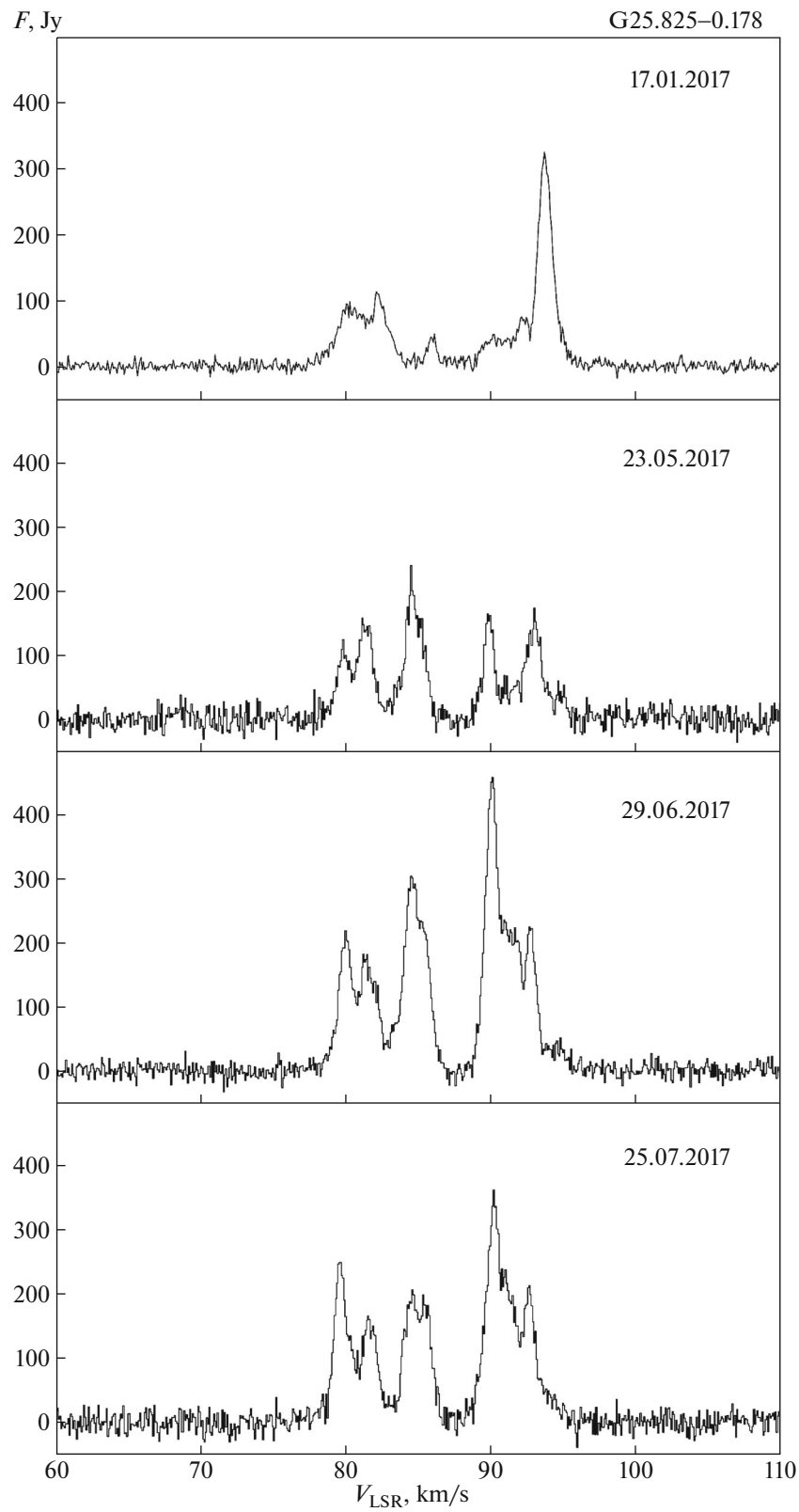


Fig. 9. Same as Fig. 8 for G25.825–0.178.

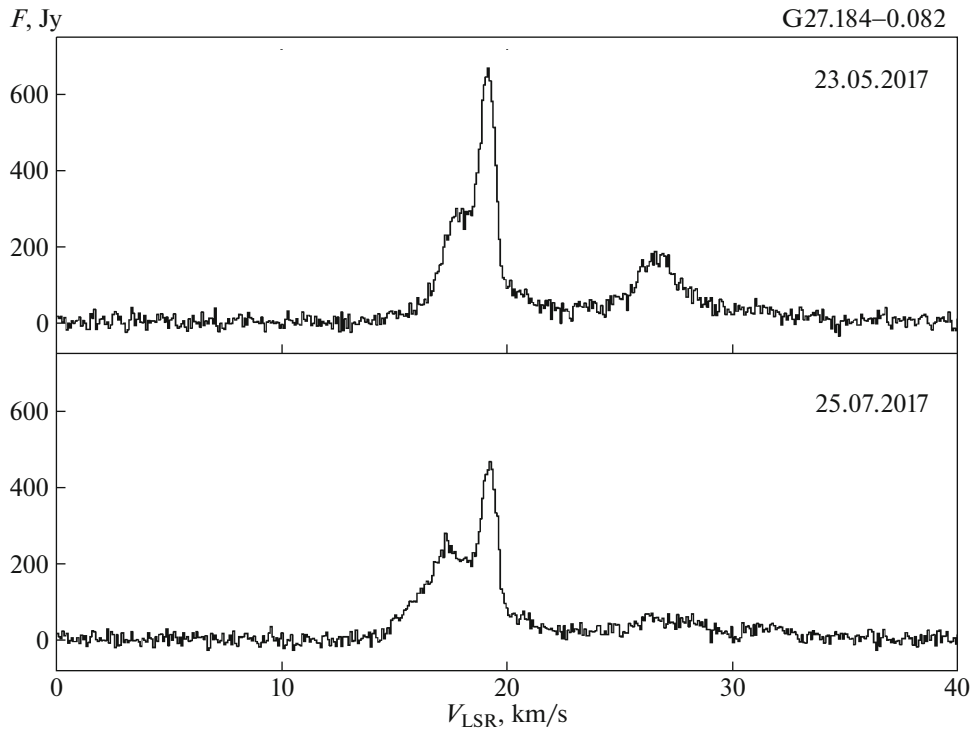


Fig. 10. Same as Fig. 8 for G27.184–0.082.

the source was overall weak: the brightest line, with velocity $V_{\text{LSR}} = 31$ km/s, had a peak flux density of only 12 Jy.

Observations in 2015–2017 on the PRAO 22-m telescope showed that the source was fairly bright in 2015: there was only one feature in the spectrum, with a velocity of 31 km/s and a flux density of 400–500 Jy. The spectrum had two closely spaced lines with $V_{\text{LSR}} \sim 31$ km/s with flux densities of less than 100 Jy during November 2016–January 2017. Figure 12 presents a spectrum of G35.20 obtained on the PRAO 22-m telescope in July 2017.

In observations on the CrAO 22-m telescope extending over five months, the brightness of the source did not exceed 200 Jy, apart from the last spectrum. In September, the spectrum had three closely spaced maser features at velocities of 30, 31, and 31.5 km/s with flux densities of 600, 400, and 500 Jy, respectively (see Fig. 5).

5.6. G43.8–0.13

The source G43.8–0.13 (further G43.8) was monitored during 1987–2007 on the Medicina 32-m telescope [52], and remained fairly bright during this entire 20-year period: the minimum peak flux density of the brightest feature in the spectrum was 300 Jy in 2007. The maximum flux density, about 4000 Jy at the peak, was observed in 1990, when the integrated

flux from all the spectral components also displayed its maximum value over the observed period, about 7000 Jy km/s. The brightness of G43.8 subsequently decreased, with the integrated brightness in 1998 being modest (see [52, Fig. A.25.d]).

The H₂O maser G43.8 was studied during an extended period of monitoring of H₂O masers with the PRAO 22-m telescope starting in 1981 [54]. This source has remained bright for many years, and consistently displays an interesting spectrum. The peak flux density of the brightest feature, at 37.5 km/s, exceeded 500 Jy during 1994–1998, and exceeded 1000 Jy during 2016–2017, reaching nearly 3000 Jy on January 16, 2017. Three other lines with $V_{\text{LSR}} = 34$, 38, and 40.5 km/s and flux densities of 300–500 Jy are also present in spectra obtained in 2016–2017. Figure 13 presents spectra of G43.8 obtained on the PRAO 22-m telescope in May–July 2017.

During monitoring with the CrAO 22-m telescope, the main line had flux densities of 1200–2200 Jy, but this flux density decreased to 360 Jy in September 2017. Note that the feature at $V_{\text{LSR}} = 34$ km/s is absent from the spectrum of G43.8 during nearly the entire observing period apart from the last month, when it again appeared with a flux density of about 100 Jy. The line with $V_{\text{LSR}} = 40.5$ km/s was always present with a flux density of 200–500 Jy (see Fig. 6).

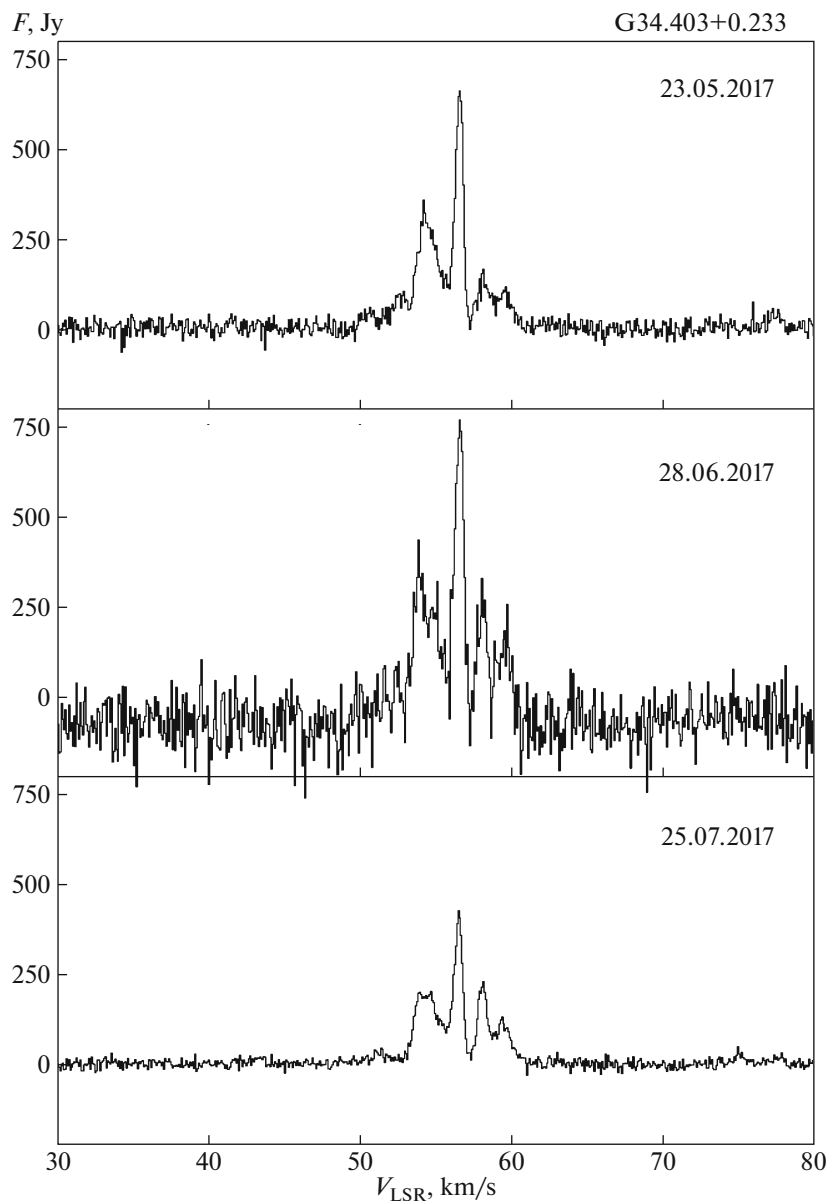


Fig. 11. Same as Fig. 8 for G34.403+0.233.

This source was observed at 22 GHz on RadioAstron in May–June 2015; fringes were detected on a space–ground baseline with a length of 0.9 Earth diameters, with the flux density of a compact feature less than $240 \mu\text{as}$ (≈ 2.7 AU at a distance of 11.8 kpc) in size being ≈ 150 Jy [55].

5.7. G107.3+5.64

The H_2O maser G107.3+5.64 (further G107.3) was observed in 1988 on the Effelsberg 100-m telescope and in 1991 on the 32-m Medicina telescope [56]. The Effelsberg spectra displayed three features with $V_{\text{LSR}} = -20.8$, -22.4 , and -24.3 km/s and peak flux densities of 260, 220, and 100 Jy,

respectively [56]. The spectrum of G107.3 observed with the Medicina 32-m telescope was variable [56]: of these three lines, only the central one remained, but another feature with a flux density of 100 Jy appeared at -20 km/s.

The source was also monitored on the Medicina 32-m antenna during 1989–2007 [52]; during this entire period, the source displayed appreciable variability in both its maximum brightness (10–800 Jy) and the number and velocities of the components in the spectrum. The appearance of the spectrum underwent appreciable variations on time scales of several months, with one to seven features present at different periods, and with some features completely disappearing while new features appeared (see

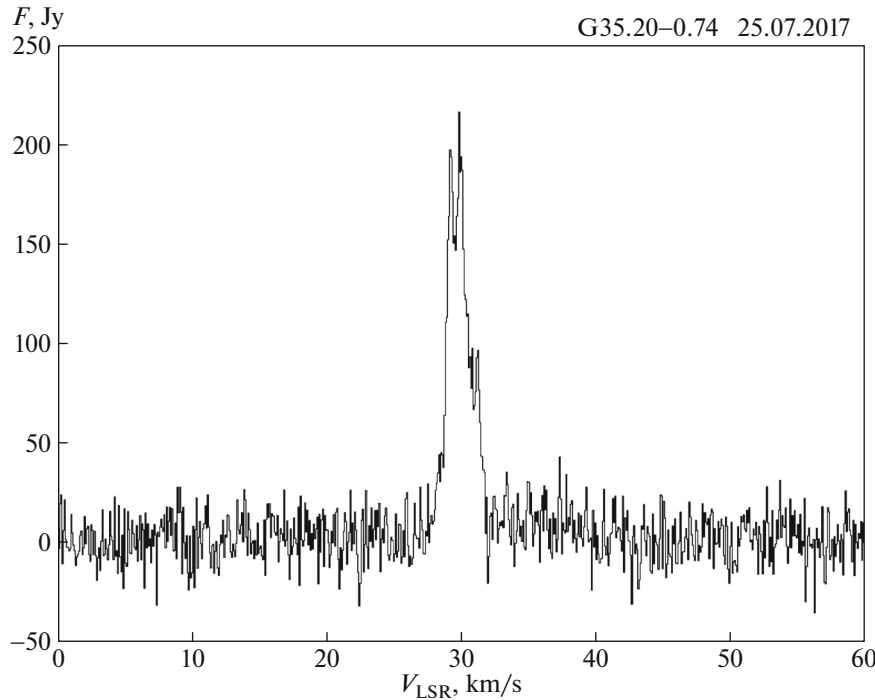


Fig. 12. Same as Fig. 8 for G35.20–0.74.

the spectra in [52, Fig. A.37.a]). It is interesting that, during 1989–2007, the brightest components in the spectrum of G107.3 were located at velocities from -15 to -20 km/s, substantially different from the systematic velocity for the molecular cloud with which G107.3 is associated, $V_{\text{therm}} = -10.1$ km/s.

Observations on the PRAO 22-m telescope in 2016–2017 showed the presence of maser features at velocities of -17.5 , -16.5 , and -7 km/s with flux densities of 140, 50, and 170 Jy, respectively. The flux density at $V_{\text{LSR}} = -17$ km/s had risen to 600 Jy two months later, in January 2017. Figure 14 presents spectra of G107.3 obtained on the PRAO 22-m telescope in May–July 2017.

Subsequent monitoring of the source on the CrAO 22-m telescope did not indicate any cardinal variations in the spectrum. The flux density of a feature at -17 km/s that flared to 600 Jy displayed a tendency to decrease to 200 Jy during this observing period, starting from April 2017 (see Fig. 7).

6. DISCUSSION

All the sources display fairly strong variability on time scales of several months, suggesting the presence of compact structures (maser spots) in these objects, making them interesting for interferometric observations. This is also supported by the calculated linear sizes of such structures in G34.403 and G43.8

based on the results of ground-based and space-ground interferometry presented above, about 2 AU.

The flux densities of various components observed in the spectra over five months range from ~ 40 to ~ 2300 Jy. A flare reaching $\sim 17\,000$ Jy at 42.8 km/s was observed in G25.65+1.05 on September 7, 2017, which subsequently increased to 60 000 Jy at the end of September 2017. Most of the maser features in the spectra have peak flux densities of 200–400 Jy, on average, satisfying the observational criterion for inclusion in our sample (flux densities exceeding 200 Jy).

Figure 15 presents for each source the time dependence of the integrated flux density in all spectral components (upper panels) and of the flux density of the maximum peak (lower panels). These plots illustrate the general activity of the masers over the entire observing period. As can be seen in Fig. 15, G25.65, G25.825, and G35.20 display a tendency for the integrated flux density to grow over the entire spectrum over the entire observed period, while the integrated brightnesses of G27.184, G34.403, and G43.8 gradually decreased. The integrated brightness of G107.3 both rose and fell in the observed period, as is also the case for the flux density of the maximum peak. As a rule, the variations in the integrated flux density correlate with the variations of the flux density in the brightest feature, with the exception of G27.184 and G34.403, in which these two sets of variations are anti-correlated during most of the observed period. This may suggest that the increase (or decrease)

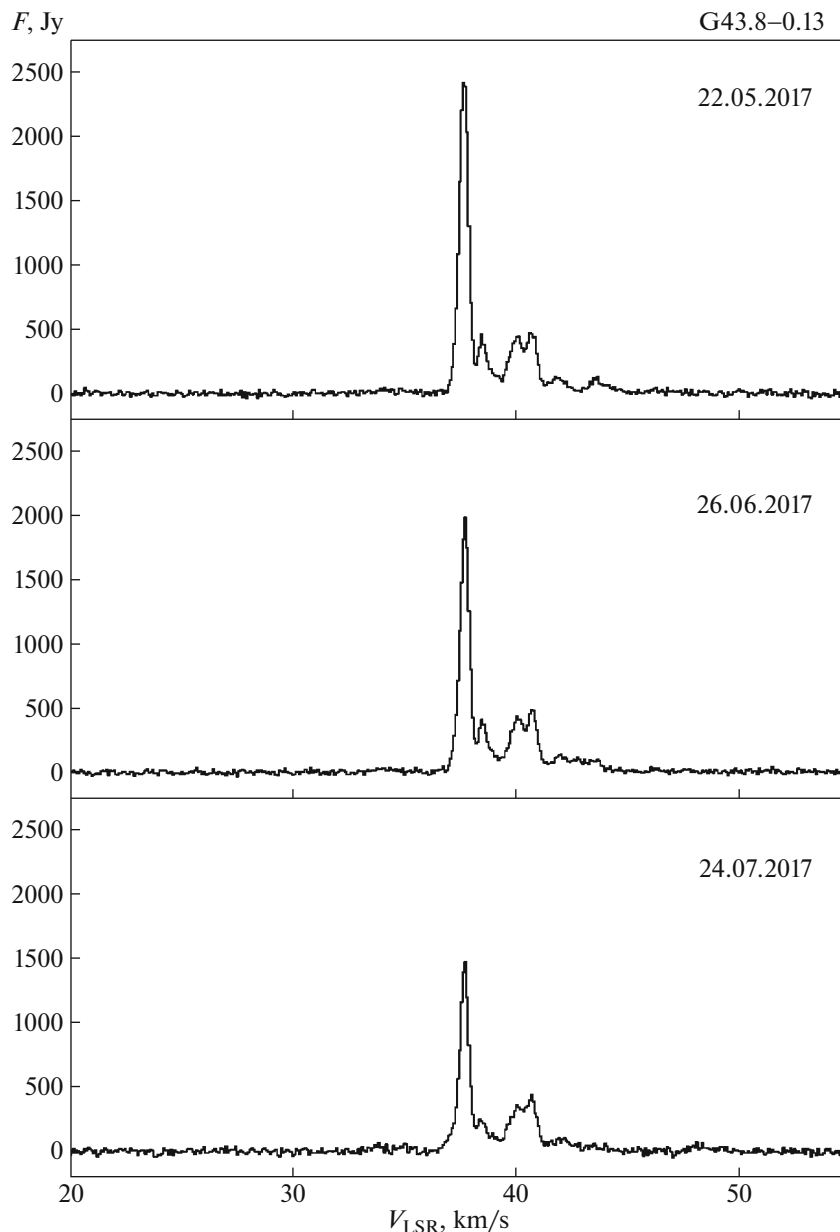


Fig. 13. Same as Fig. 8 for G43.8–0.13.

in the integrated brightnesses in these sources occurred due to a brightening (or dimming) of several components simultaneously, rather than to variations of one bright feature; i.e., the integrated brightness variations were due to overall activity of the source (G34.403). Another origin could be the appearance of new features in the spectrum (G27.184). In the former case, the overall growth in the flux in all spectral features indicates variations in the conditions for pumping by an external source, for example, an increase in the infrared flux in the central part of the region due to the accretion of matter [57]. Testing this hypothesis requires longer series of observations sup-

plemented by observations in other spectral ranges. In the latter case, the appearance of new features in the spectrum could be due, for example, to turbulent motions of matter or precession of a disk causing its position relative to the plane of the sky to vary, leading to variations in the thickness of a gaseous layer long the line of sight.

Analysis of spectra obtained on the CrAO 22-m telescope (Figs. 1–7) shows that the velocity range occupied by the various components in the source spectra is 5–20 km/s. For two of the sources, the velocity scatter of the features is about 5 km/s (G35.20, G107.3), and this scatter is about 10 km/s for two

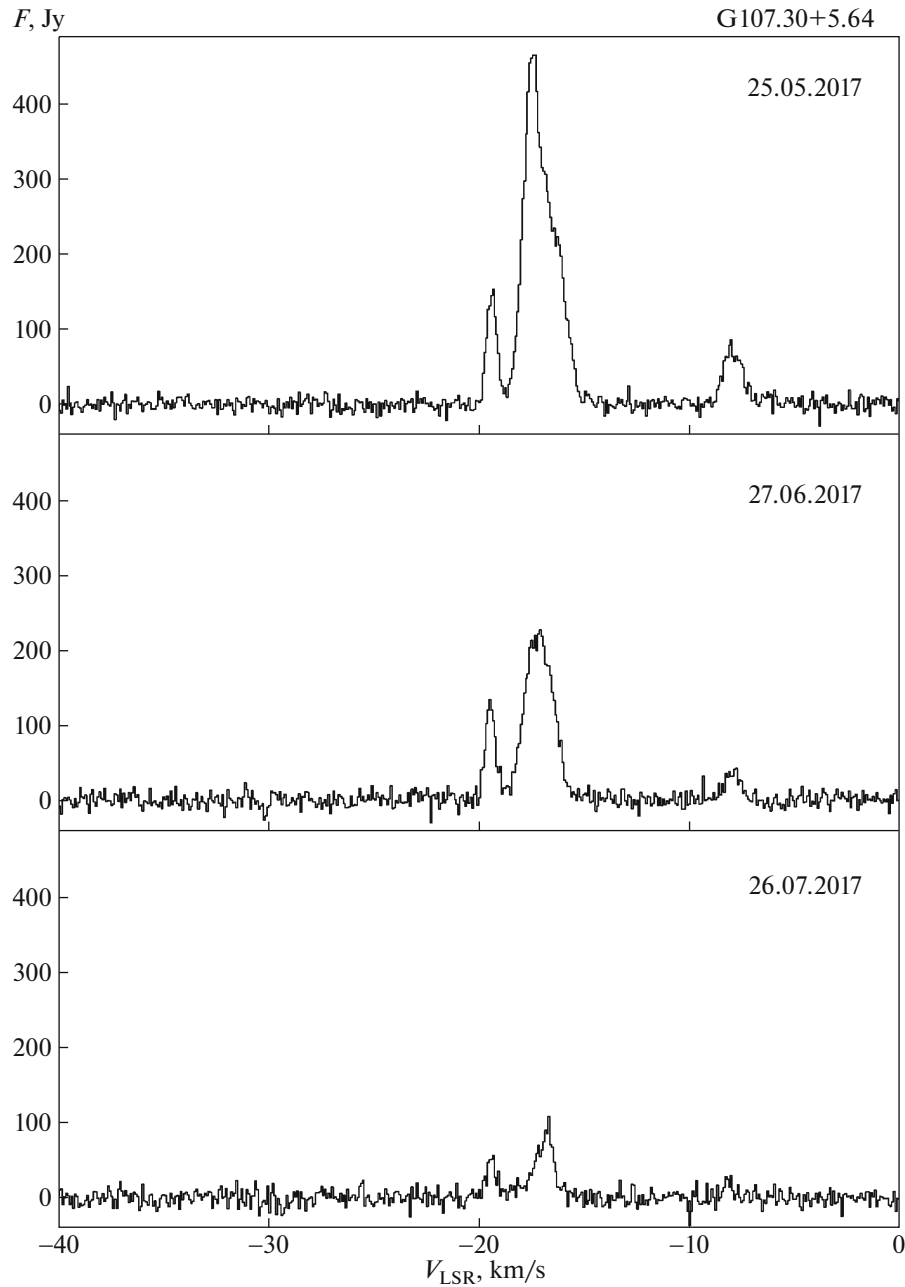


Fig. 14. Same as Fig. 8 for G107.30+5.64.

others (G34.403, G43.8). The widths of thermal lines observed in star-forming regions and the associated gas–dust condensations in such regions can comprise 2–15 km/s (see, e.g., [29]). Thus, the scatter of the maser-feature velocities of 5–10 km/s may indicate that the structures responsible for the maser radiation in the various components in a given source are arranged fairly close to each other in space within a single star-forming region (i.e., possibly in a single gas–dust condensation).

The velocity scatter of the features in G27.184 is 15 km/s, and this scatter is about 20 km/s two

other sources (G25.65, G25.825). Such scatters may indicate the presence of possible dynamical effects in the region. For example, the appearance of a strong, variable flare in G25.65 could correspond to a strong fountain/stream of matter or the ejection of a bipolar outflow from the central object into the outer layer of the blue front. At the same time, the preservation of stable positions for the bright maser features in the blue part of the spectrum provides evidence for the presence of a stable spatial structure such as the edge of a disk, not an outflow of matter in the form of a stream from the central object. During the time

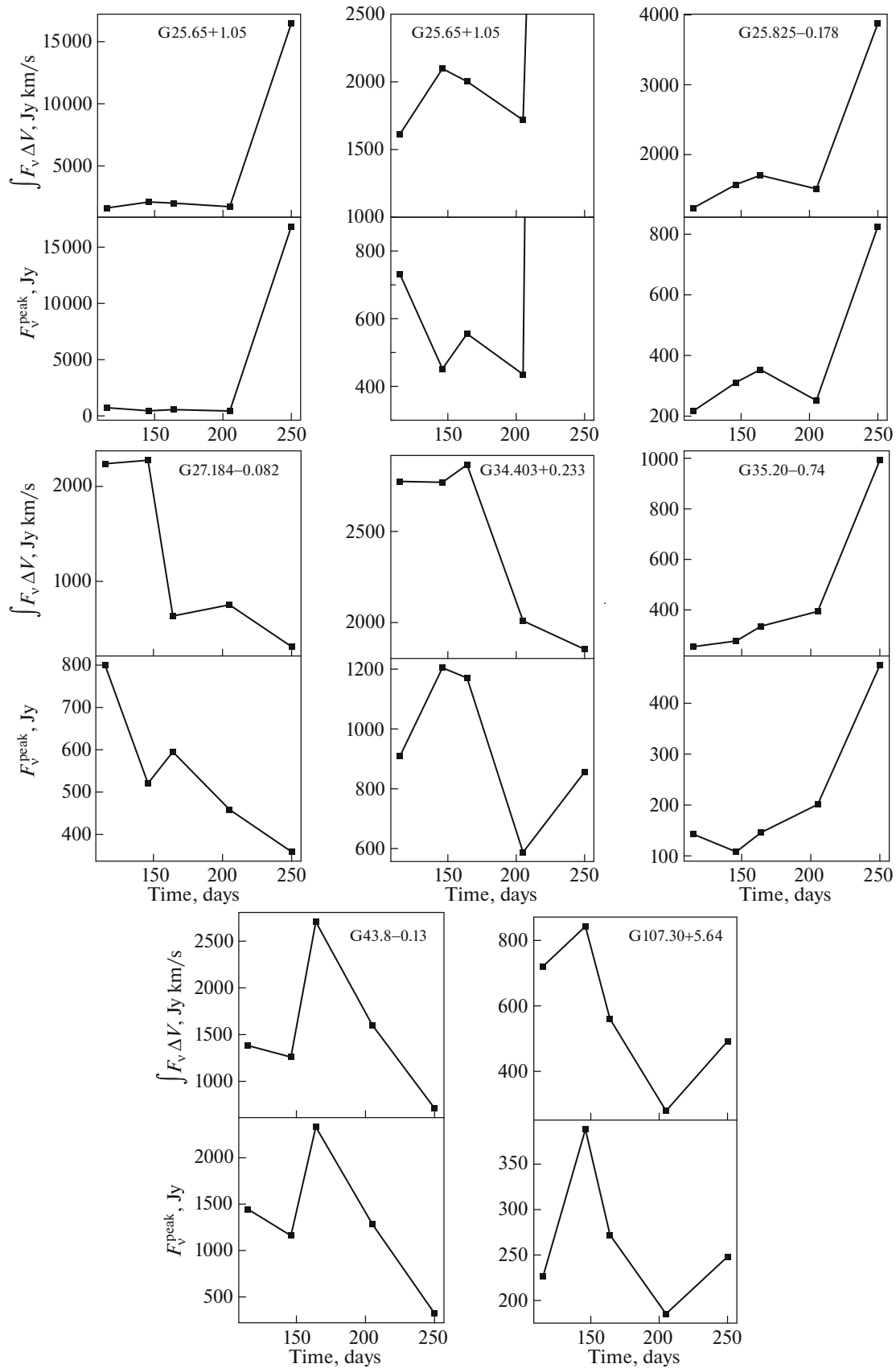


Fig. 15. Dependence of the integrated flux density (upper panels) and the flux density of the highest peak in the spectrum (lower panels) on the observing date.

covered by our observations, G25.65 displayed very powerful flares in which the flux density of the main maser feature grew by a factor of several hundred relative to the “quiescent” state. These flares may be associated with processes in the circumstellar disk. We referred to one possibility above—a growth in the flux of IR radiation in the central part of the region during an enhancement in the accretion of matter onto the central stellar object [57], or the action of a shock arising in such an accretion episode on the maser region. A maser can also flare, for example, when two or more protoplanetary maser condensations moving in Keplerian orbits around the central object and amplifying the H₂O emission in the unsaturated regime become aligned along the line of sight. This type of model was proposed in [58] to explain a power H₂O maser flare in Orion A. Other possibilities could be a favorable orientation of protoplanetary rings in a disk [59], or alignment along the line of sight of the axis of a maser filament arising in a disk due to gravitational instability [60].

More extended flux-density monitoring and mapping of maser features in various molecular transitions in these types of sources will help distinguish between these various scenarios.

7. CONCLUSION

1. We have carried out monitoring of seven H₂O maser sources in regions in which massive stars are forming, analyzed the resulting observational data, and compared spectra obtained with data from earlier studies.

2. The equipment used on the CrAO 22-m telescope operates in a standard regime, and the calibration enables comparison with similar observations carried out on the PRAO 22-m telescope and other single dishes.

3. All the H₂O maser sources observed in our study display strong variability, which presents problems for planning interferometric observations. On the other hand, this variability shows the need for observations and monitoring with single dishes in preparation for interferometric observations, since this enables estimation of the flux densities of maser features, the mean flux in the main feature in the spectrum, and the time scale for stability of the flux density. All this information is of fundamental importance for planning observations involving a large number of antennas and optimizing the useful observing time.

4. Our monitoring in September 2017 revealed a maser flare in G25.65+1.05, which provided the motivation for rapidly organizing interferometric observations with RadioAstron.

ACKNOWLEDGMENTS

We thank the staff of the 22-m telescopes of the Crimean Astrophysical Observatory and the Pushchino Radio Astronomy Observatory for their help in carrying out these observations. This work was partially supported by Program 28 of the Russian Academy of Sciences, “The Cosmos: Fundamental Processes and Their Interconnections,” and the Russian Foundation for Basic Research (grant 18-42-910018).

REFERENCES

1. E. E. Lekht, V. V. Krasnov, and A. M. Tolmachev, *Astron. Lett.* **40**, 551 (2014).
2. P. Colom, E. E. Lekht, M. I. Pashchenko, G. M. Rudnitskii, and A. M. Tolmachev, *Astron. Rep.* **60**, 730 (2016).
3. T. R. Hunter, C. L. Brogan, G. MacLeod, C. J. Cyganowski, et al., *Astrophys. J.* **837**, L29 (2017).
4. <http://www.asc.rssi.ru/radioastron/index.html>.
5. H. S. Kardashev, A. V. Alakoz, A. S. Andrianov, M. I. Artyukhov, et al., *Vestn. FGUP NPO Lavochkina* **3**, 4 (2016).
6. Bayesian Distance Calculator. <http://bessel.vlbi-astrometry.org/bayesian>.
7. A. J. Walsh, A. R. Hyland, G. Robinson, and M. G. Burton, *Mon. Not. R. Astron. Soc.* **291**, 261 (1997).
8. M. A. Braz, J. C. Gregorio Hetem, E. Scalise, Jr., J. L. Monteiro Do Vale, and M. Gaylard, *Astron. Astrophys. Suppl. Ser.* **77**, 465 (1989).
9. T. Kurayama, A. Nakagawa, S. Sawada-Satoh, K. Sato, M. Honma, K. Sunada, T. Hirota, and H. Imai, *Publ. Astron. Soc. Jpn.* **63**, 513 (2011).
10. B. Zhang, X. W. Zheng, M. J. Reid, K. M. Menten, Y. Xu, L. Moscadelli, and A. Brunthaler, *Astrophys. J.* **693**, 419 (2009).
11. J. Forster and J. Caswell, *Astron. Astrophys.* **213**, 339 (1989).
12. A. Palau, A. Fuente, J. M. Girart, R. Estalella, et al., *Astrophys. J.* **762**, 120 (2013).
13. A. Zavagno, L. Deharveng, D. Nadeau, and J. Caplan, *Astron. Astrophys.* **394**, 225 (2002).
14. S. Kurtz, E. Churchwell, and D. O. S. Wood, *Astrophys. J. Suppl.* **91**, 659 (1994).
15. Á. Sánchez-Monge, M. T. Beltrán, R. Cesaroni, S. Etoka, et al., *Astron. Astrophys.* **569**, A11 (2014).
16. M. J. Gaylard, G. C. MacLeod, and D. J. van der Walt, *Mon. Not. R. Astron. Soc.* **269**, 257 (1994).
17. O. S. Bayandina, I. E. Val’tts, S. E. Kurtz, and N. N. Shakhvorostova, (2018, in preparation).
18. F. Fontani, R. Cesaroni, and R. S. Furuya, *Astron. Astrophys.* **517**, 56 (2010).
19. G. Surcis, W. H. T. Vlemmings, H. J. van Langevelde, B. Hutawarakorn Kramer, A. Bartkiewicz, and M. G. Blasi, *Astron. Astrophys.* **578**, 102 (2015).

20. E. Rosolowsky, M. K. Dunham, A. Ginsburg, E. Bradley, et al., *Astrophys. J. Suppl.* **188**, 123 (2010).
21. V. Rosero, P. Hofner, S. Kurtz, J. Biegging, and E. D. Araya, *Astrophys. J. Suppl.* **207**, 12 (2013).
22. E. D. Araya, P. Hofner, W. M. Goss, H. Linz, S. Kurtz, and L. Olmi, *Astrophys. J. Suppl.* **178**, 330 (2008).
23. M. Szymczak and E. Gérard, *Astron. Astrophys.* **414**, 235 (2004).
24. O. S. Bayandina, I. E. Val'tts, and S. E. Kurtz, *Astron. Rep.* **59**, 997 (2015).
25. M. R. Pestalozzi, V. Minier, and R. S. Booth, *Astron. Astrophys.* **432**, 737 (2005).
26. Y. Wu, C. Henkel, R. Xue, X. Guan, and M. Miller, *Astrophys. J.* **669**, 37 (2007).
27. D. J. van der Walt, *Astron. Astrophys. Suppl. Ser.* **110**, 81 (1995).
28. J. L. Caswell, R. A. Vaile, S. P. Ellingsen, J. B. Whiteoak, and R. P. Norris, *Mon. Not. R. Astron. Soc.* **272**, 96 (1995).
29. L. Bronfman, L.-A. Nyman, and J. May, *Astron. Astrophys. Suppl. Ser.* **115**, 81 (1996).
30. W. M. Schlingman, Y. L. Shirley, D. E. Schenk, E. Rosolowsky, et al., *Astrophys. J. Suppl.* **195**, 14 (2011).
31. C. J. Cyganowski, B. A. Whitney, E. Holden, E. Braden, et al., *Astron. J.* **136**, 2391 (2008).
32. G. Surcis, W. H. T. Vlemmings, H. J. van Langevelde, and B. Hutawarakorn Kramer, *Astron. Astrophys.* **541**, A47 (2012).
33. R. Bachiller, K. M. Menten, J. Gómez-González, and A. Barcia, *Astron. Astrophys.* **240**, 116 (1990).
34. D. S. Shepherd and E. Churchwell, *Astrophys. J.* **457**, 267 (1996).
35. A. L. Argon, M. J. Reid, and K. M. Menten, *Astrophys. J. Suppl.* **129**, 159 (2000).
36. F. Palla, J. Brand, G. Comoretto, M. Felli, and R. Cesaroni, *Astron. Astrophys.* **246**, 249 (1991).
37. Á. Sánchez-Monge, A. Palau, R. Estalella, M. T. Beltrán, and J. M. Girart, *Astron. Astrophys.* **485**, 497 (2008).
38. I. G. Moiseev and N. S. Nesterov, *Izv. Krymsk. Astrofiz. Observ.* **73**, 154 (1985).
39. J. Brand, R. Cesaroni, P. Caselli, M. Catarzi, et al., *Astron. Astrophys. Suppl. Ser.* **103**, 541 (1994).
40. S. Kurtz and P. Hofner, *Astron. J.* **130**, 711 (2005).
41. E. E. Lekht, M. I. Pashchenko, G. M. Rudnitskij, and A. M. Tolmachev, *Astron. Rep.* **62**, 213 (2018).
42. A. E. Volvach, L. N. Volvach, G. MacLeod, E. E. Lekht, G. M. Rudnitskij, and A. M. Tolmachev, *Astron. Telegram*, No. 10728 (2017).
43. A. J. Walsh, S. L. Breen, T. Britton, K. J. Brooks, et al., *Mon. Not. R. Astron. Soc.* **416**, 1764 (2011).
44. A. J. Walsh, C. R. Purcell, S. N. Longmore, S. L. Breen, J. A. Green, L. Harvey-Smith, C. H. Jordan, and C. Macpherson, *Mon. Not. R. Astron. Soc.* **442**, 2240 (2014).
45. J. S. Urquhart, L. K. Morgan, C. C. Figura, T. J. T. Moore, et al., *Mon. Not. R. Astron. Soc.* **418**, 1689 (2011).
46. C. J. Cyganowski, J. Koda, E. Rosolowsky, S. Towlers, J. Donovan Meyer, F. Egusa, R. Momose, and T. P. Robitaille, *Astrophys. J.* **764**, 61 (2013).
47. Y. Wang, Q. Zhang, J. M. Rathborne, J. Jackson, and Y. Wu, *Astrophys. J.* **651**, L125 (2006).
48. T. Kurayama, in *Approaching Micro-Arcsecond Resolution with VSOP-2: Astrophysics and Technologies*, Ed. by Y. Hagiwara, E. Fomalont, M. Tsuboi, and Y. Murata, *ASP Conf. Ser.* **402**, 473 (2009).
49. A. Lobanov, *Astron. Astrophys.* **574**, A84 (2015).
50. G. M. Rudnitskii, E. E. Lekht, O. S. Bayandina, I. E. Val'tts, and E. R. Khan, *Astron. Rep.* **60**, 129 (2016).
51. L. T. Little, A. T. Brown, P. W. Riley, N. Matthews, G. H. MacDonald, D. R. Vizard, and R. J. Cohen, *Mon. Not. R. Astron. Soc.* **203**, 409 (1983).
52. M. Felli, J. Brand, R. C. Cesaroni, C. Codella, et al., *Astron. Astrophys.* **476**, 373 (2007).
53. R. Valdetaro, F. Palla, J. Brand, R. Cesaroni, G. Comoretto, M. Felli, and F. Palagi, *Astron. Astrophys.* **383**, 244 (2002).
54. E. E. Lekht and R. L. Sorochenko, *Astron. Rep.* **76**, 758 (1999).
55. A. M. Sobolev, N. N. Shakhvorostova, A. V. Alakoz, and W. A. Baan, in *Stars: From Collapse to Collapse*, Ed. by Yu. Yu. Balega, D. O. Kudryavtsev, I. I. Romanyuk, and I. A. Yakunin (ASP, San Francisco, 2007), p. 27.
56. J. G. A. Wouterloot, J. Brand, and K. Fiegle, *Astron. Astrophys. Suppl. Ser.* **98**, 589 (1993).
57. A. Caratti o Garatti, B. Stecklum, R. Garcia Lopez, et al., *Nat. Phys.* **13**, 276 (2017).
58. V. S. Strel'nitskii, *Sov. Astron. Lett.* **8**, 86 (1982).
59. L. I. Matveenko, *Sov. Astron. Lett.* **7**, 54 (1981).
60. R. T. Tominaga, S. Inutsuka, and S. Z. Takahashi, *Publ. Astron. Soc. Jpn.* **70**, 3 (2018); arXiv:1711.05948.
61. M. Szymczak, M. Olech, P. Wolak, A. Bartkiewicz, M. Gawroński, *Mon. Not. R. Astron. Soc.* **459**, 56 (2016).

Translated by D. Gabuzda